DRP1-mediated mitochondrial fission is essential to maintain cristae morphology and bioenergetics

Gabriella L. Robertson[1], Stellan N. Riffle[1], Mira Patel[1], Andrea Marshall[2], Heather Beasley[2], Edgar Garza Lopez[2], Jianqiang Shao[3], Zer Vue[2], Antentor Hinton Jr.[2], Jason A. Mears[4], and Vivian Gama[1, 5,6,7]

[1]Vanderbilt University, Cell and Developmental Biology, Nashville, TN.
[2]Vanderbilt University, Molecular Physiology and Biophysics, Nashville, TN.
[3]Central Microscopy Research Facility, University of Iowa, Iowa City, IA.
[4]Case Western Reserve University, Department of Pharmacology and Center for Mitochondrial Diseases, Cleveland, OH.
[5]Vanderbilt University, Vanderbilt Center for Stem Cell Biology, Nashville, TN
[6]Vanderbilt University, Vanderbilt Brain Institute, Nashville, TN

[7]Corresponding author

Correspondence should be addressed to:

Vivian Gama
PMB407935
465 21st Avenue South, 4150A
Vanderbilt University
Nashville, TN 37240-7935
Tel: (615) 875-9490
vivian.gama@vanderbilt.edu

Running title: DRP1 mutations associated with EMPF1

Keywords: fibroblasts, DRP1, mitochondria, peroxisomes, cristae, glycolysis, oxidative phosphorylation

Abstract

Mitochondria and peroxisomes are both dynamic signaling organelles that constantly undergo fission. While mitochondrial fission is known to coordinate cellular metabolism, proliferation, and apoptosis, the physiological relevance of peroxisome dynamics and the implications for cell fate are not fully understood. DRP1 (dynamin-related protein 1) is an essential GTPase that executes both mitochondrial and peroxisomal fission. Patients with *de novo* heterozygous missense mutations in the gene that encodes DRP1, *DNM1L*, present with encephalopathy due to defective mitochondrial and peroxisomal fission (EMPF1). EMPF1 is a devastating neurodevelopmental disease with no effective treatment. To interrogate the mechanisms by which DRP1 mutations cause cellular dysfunction, we utilized human-derived fibroblasts from patients with mutations in DRP1 who present with EMPF1. As expected, patient cells display elongated mitochondrial morphology and lack of fission. Patient cells display a lower coupling efficiency of the electron transport chain, increased proton leak, and upregulation of glycolysis. In addition to these metabolic abnormalities, mitochondrial hyperfusion results in aberrant cristae structure and hyperpolarized mitochondrial membrane potential, both of which are tightly linked to the changes in metabolism. Peroxisome structure is also severely elongated in patient cells and results in a potential functional compensation of fatty acid oxidation. Understanding the mechanism by which DRP1 mutations cause these metabolic changes will give insight into the role of mitochondrial dynamics in cristae maintenance and the metabolic capacity of the cell, as well as the disease mechanism underlying EMPF1.

54 **Introduction**

55 Mitochondrial dynamics are controlled and executed by a vast group of proteins and other
56 organelles. The underlying morphology of the mitochondria is an important determinant for the
57 ability of this organelle to regulate a variety of cellular processes, such as apoptosis, cell fate, lipid
58 biosynthesis, and epigenetic modifications (Vantaggiato *et al*, 2019; Khacho *et al*, 2016; Iwata *et*
59 *al*, 2020; Bayraktar *et al*, 2019; King *et al*, 2021; Prigione & Adjaye, 2011; Rasmussen *et al*, 2020).
60 Mitochondrial fusion is primarily catalyzed by the large GTPases Mitofusin 1 and Mitofusin 2 at
61 the outer mitochondrial membrane (Chen *et al*, 2003). The GTPase OPA1 is responsible for
62 executing fusion of the inner mitochondrial membrane (Delettre *et al*, 2000; Alexander *et al*, 2000).
63 Mitochondrial fission, mediated through the large GTPase DRP1 (Dynamin-related protein 1), is
64 orchestrated by a complex sequence of events (Smirnova *et al*, 2001; Fonseca *et al*, 2019). The
65 first steps of mitochondrial fission include contact with the endoplasmic reticulum (ER) and
66 replication of the mitochondrial genome (Lewis *et al*, 2016; Friedman *et al*, 2011). This is followed
67 by contact and pre-constriction by actin filaments, which are associated with the ER membrane
68 (Li *et al*, 2015; Ji *et al*, 2015, 2017; Chakrabarti *et al*, 2018; Hatch *et al*, 2016, 2014). Fission is
69 also regulated through adaptor proteins at the outer mitochondrial membrane, including MiD49,
70 MiD51, MFF, and FIS1; however, their distinct roles in fission are not completely understood
71 (Osellame *et al*, 2016; Palmer *et al*, 2013; Losó n *et al*, 2013). After the association with adaptor
72 proteins, DRP1 then forms a multimeric ring around the mitochondria and hydrolyzes GTP to
73 GDP, causing a confirmational change in the ring that executes fission (Chang & Blackstone,
74 2007; Fröhlich *et al*, 2013; Nagashima *et al*, 2020; Francy *et al*, 2015; Wang *et al*, 2018; Kamerkar
75 *et al*, 2018). DRP1 is essential for mitochondrial fission, and without functional DRP1 the
76 mitochondrial network becomes hyperfused. In addition to the effects on mitochondrial
77 morphology, DRP1 also mediates the fission of peroxisomes (Koch *et al*, 2003). Peroxisomes are
78 highly specialized organelles vital for the beta oxidation of very-long-chain fatty acids,

79 detoxification of reactive oxygen species (ROS), production of cholesterol, bile acids, and
80 plasmalogens, which contribute to the phospholipid content in the brain white matter (Schrader *et*
81 *al*, 2020; Ravi *et al*, 2021; Ding *et al*, 2021; Lodhi & Semenkovich, 2014; Ferreira *et al*, 2021;
82 Chandel, 2021; Sugiura *et al*, 2017). The adaptor proteins MFF and FIS1 are also involved in
83 DRP1 recruitment to sites of peroxisome fission (Gandre-Babbe & Van Der Bliek, 2008; Itoyama
84 *et al*, 2013; Koch & Brocard, 2012). The contacts between mitochondria and peroxisomes are
85 essential for linking peroxisomal β-oxidation and mitochondrial ATP generation by the ETC,
86 maintenance of redox homeostasis, and lipid transfer (Fransen *et al*, 2017; Fan *et al*, 2016;
87 Chandel, 2021). Thus, the metabolic activity of peroxisomes and mitochondria are functionally
88 interconnected. Consistent with this, peroxisomal disorders caused by mutations in genes
89 involved in the biogenesis and function of peroxisomes are often associated with mitochondrial
90 dysfunction (Tanaka *et al*, 2019). This connection may be particularly important during brain
91 development and metabolic stress. However, the molecular mechanisms that facilitate this
92 communication are still poorly understood.

93 In mouse models, global DRP1 knockout is embryonic lethal (Wakabayashi *et al*, 2009; Ishihara
94 *et al*, 2009). With the advent of exome sequencing, patients with *de novo* mutations in the gene
95 that encodes DRP1, *DNM1L (Dynamin 1 Like)*, have been identified (Waterham *et al*, 2007; Chao
96 *et al*, 2016; Fahrner *et al*, 2016; Sheffer *et al*, 2016; Ryan *et al*, 2018; Liu *et al*, 2021; Nasca *et al*,
97 2016; Vandeleur *et al*, 2019; Nolan *et al*, 2019; Keller *et al*, 2021; Longo *et al*, 2020). The disease
98 associated with mutations in *DNM1L* is known as encephalopathy due to defective mitochondrial
99 and peroxisomal fission-1 (EMPF1). Most reported mutations are heterozygous missense, and
100 patients present with heterogeneous symptoms including neurodevelopmental delay, seizures,
101 muscle abnormalities, and ataxia. Patient fibroblasts show very elongated mitochondrial networks
102 and elevated lactate levels, suggesting an impairment in oxidative phosphorylation (Liu *et al*,
103 2021; Whitley *et al*, 2018). Currently, there is no effective treatment or cure for patients effected

104 by DRP1 mutations, and the life expectancy for most patients with DRP1 mutations is childhood
105 to early adolescence (Ryan *et al*, 2018). Although other proteins are involved in fission, DRP1
106 has been shown to be indispensable for mitochondrial fission (Smirnova *et al*, 2001; Kamerkar *et*
107 *al*, 2018; Fonseca *et al*, 2019; Nagashima *et al*, 2020; Csordás *et al*, 2006; Li *et al*, 2015), yet the
108 cellular consequences of DRP1 dysfunction are not well understood. In this study, we aimed to
109 characterize the effects of two mutations in DRP1 identified in patients with EMPF1: the G32A
110 mutation, which lies in the catalytic GTPase domain of DRP1, and the R403C mutation, which
111 lies in the stalk domain (Fröhlich *et al*, 2013). We resolved and quantified mitochondrial and
112 peroxisomal morphological features associated with EMPF1-associated mutations and reveal
113 their impact on cellular metabolism to put into perspective previously described clinical findings
114 (Ryan *et al*, 2018; Fahrner *et al*, 2016; Liu *et al*, 2021) and gain fundamental insight into the
115 metabolic adaptations to dysfunctional organelle fission. We found that the inability of DRP1 to
116 fragment the mitochondria in patient-derived fibroblasts leads not only to the hyperfusion
117 phenotype previously described, but also to delayed cell death in response to apoptotic signals,
118 aberrant mitochondrial cristae structure, and hyperpolarized mitochondrial membrane potential.
119 Metabolically, the changes in mitochondrial and peroxisomal morphology result in inefficiency of
120 the electron transport chain coupling oxygen consumption with ATP production and upregulation
121 of glycolysis. Altogether, these data indicate that mitochondrial and peroxisomal fission influence
122 dynamics of the inner mitochondrial membrane and the metabolic state of the cell.

123

Results

DRP1 variants found in patients have dominant negative effects that alter the expression of critical proteins at the mitochondria

Light microscopy studies have shown profound alterations of mitochondrial fission in cells from patients harboring mutations in DRP1 (Ryan *et al*, 2018; Whitley *et al*, 2018). These studies highlighted the clinical relevance of mitochondrial fission in neural development. We quantified the morphology of the mitochondria in patient-derived primary fibroblasts at super resolution level using structured illumination microscopy (SIM). Both G32A and R403C patient fibroblast lines showed increased mitochondrial volume, surface area and major axis length consistent with a hyperfused mitochondrial morphology as reported for DRP1 null cells (Smirnova *et al*, 2001; Kamerkar *et al*, 2018; Fonseca *et al*, 2019) (Fig. 1A-B). Live-cell imaging of mitochondria stained with MitoTracker confirmed that mitochondrial fission events are rare in patient cells compared to control fibroblasts (Supplementary Fig. 1A). High resolution three-dimensional images of control and patient fibroblasts were obtained using serial block facing-scanning electron microscopy (SBF-SEM) (Garza-Lopez *et al*, 2021). Manual segmentation and stack reconstruction of the mitochondrial networks validated the increased length and volume of the mitochondrial networks as well as increased mitochondrial complexity index (MCI) in patient fibroblasts (Fig. 1C-D). MCI is a quantitative measurement of network complexity, which takes into account both volume and surface area of the mitochondria ($MCI = SA^3 / 16\pi^2V^2$) (Vincent *et al*, 2019; Faitg *et al*, 2021). Both mutations in DRP1 result in significant alterations of the mitochondrial network with G32A fibroblasts showing slightly more severe elongation than R403C (Fig. 1D and Supplementary Fig. 1B).

Both mutations in DRP1 are found to be heterozygous in patients, suggesting that mutant DRP1 has a dominant-effect that can interfere with the ability of wild-type DRP1 to fragment the mitochondria. Previous studies have demonstrated that the GFP can interfere with the activity of

149 DRP1 (Montecinos-Franjola *et al*, 2020). Thus, we generated mCherry tagged- constructs
150 containing the patient derived mutations and expressed them in human fibroblasts homozygous
151 for endogenous wild-type DRP1. Overexpression of mCherry-DRP1-G32A and mCherry-DRP1-
152 R403C by transient transfection in wild-type fibroblasts demonstrated that, as previously
153 described (Ryan *et al*, 2018; Fahrner *et al*, 2016; Whitley *et al*, 2018), the mitochondrial
154 hyperfusion seen in patient cells is not due to the genetic background and that these mutations
155 act in a dominant negative manner (Fig. 1E-F). While both mutations of DRP1 significantly
156 impaired DRP1 function in human fibroblasts, the G32A show a slightly more severe phenotype
157 than R403C.

158 DRP1 sequestration and inactivation is thought to lead to unopposed fusion events, which
159 increase the severity of mitochondrial elongation (Palmer et al., 2013). We examined the effects
160 of DRP1 mutations on the protein expression levels of mitochondrial dynamics proteins. Both
161 Mitofusin 1 and Mitofusin 2 were expressed at lower levels in patient cells than in control cells.
162 However, there was no significant difference in the expression of OPA1 (Fig. 2A). These data
163 show that there is a reduction in the expression of mitochondrial outer membrane fusion proteins
164 in patient cells, suggesting that active mitochondrial fission promotes protein stability at the outer
165 mitochondrial membrane. These data also indicate that aberrant fission caused by DRP1
166 mutations may not alter fusion dynamics at the inner mitochondrial membrane.

167 Phosphorylation of DRP1 at Serine 616 has been proposed to be a critical determinant of DRP1
168 recruitment and activity (Koch & Brocard, 2012; Taguchi *et al*, 2007; Valera-Alberni *et al*, 2021).
169 Whether mutations in DRP1 found in patients with EMPF1 affect the levels of phosphorylation at
170 serine 616 (pS616-DRP1) has not been explored. We examined DRP1 levels in patient derived
171 fibroblasts. Although there was no significant difference in total DRP1 expression, G32A patient
172 cells expressed significantly less pS616-DRP1 (Fig. 2B). Since G32A mutation impairs DRP1
173 phosphorylation to a greater extent than the R403C mutation, the GTPase domain of DRP1 may

174 be structurally or functionally involved in interactions with kinases responsible for DRP1
175 phosphorylation. We wondered whether the expression of one copy of mutant DRP1 in patient
176 fibroblasts affected the recruitment of endogenous pS616-DRP1 to the mitochondria. To test this,
177 we quantified the recruitment of phosphorylated DRP1 to the outer mitochondrial membrane using
178 super-resolution microscopy. On average, there was no significant difference in the recruitment
179 of pS616-DRP1 to the mitochondria in patient cells and control cells (Fig. 2C-D). While in all cell
180 lines, pS616-DRP1 was found in close contact to the mitochondrial membrane, in the patient
181 fibroblasts this interaction appeared less transient. These results point to generalized stalling of
182 the fission events in patient fibroblasts.

183 The onset of apoptosis is accompanied by mitochondrial remodeling, stable association of DRP1
184 to the mitochondrial membrane, and increased fragmentation of the mitochondrial membrane
185 (Martinou & Youle, 2006; Wasiak *et al*, 2007). In DRP1 deficient cells, this remodeling of
186 mitochondria is significantly reduced and the onset of cell death is delayed (Lee *et al*, 2004). To
187 determine the effects of mitochondrial stress on mitochondrial fragmentation in patient fibroblasts,
188 we quantified changes in mitochondrial fission in response to carbonyl cyanide m-
189 chlorophenylhydrazone (CCCP) treatment. As previously shown using RNAi experiments in HeLa
190 cells (Lee *et al*, 2004), patient fibroblasts showed reduced mitochondrial fragmentation induced
191 by CCCP compared to control cells (Fig. 2E-F). Although some mitochondrial fragmentation may
192 occur, mitochondrial volume and major axis length are significantly larger in patient cells treated
193 with CCCP than control cells. During apoptosis, BAX translocates to the mitochondria and
194 cytochrome c is released to the cytosol (Smaili *et al*, 2001). When BAX is recruited to the
195 mitochondria in DRP1-depleted cells, cytochrome c release is delayed. Consistent with this,
196 patient fibroblasts show higher cell survival when treated with CCCP and etoposide as well as
197 lower caspase-3 activity than control fibroblasts when treated with STS (Supplementary Fig. 2A-
198 B). Interestingly, basal levels of both BAX and BAK are significantly reduced in patient fibroblasts

199 with mutations in DRP1 (Supplementary Fig. 2C). Levels of the anti-apoptotic protein MCL-1 were
200 significantly reduced in G32A fibroblasts but not in R403C fibroblasts, while BCL-XL expression
201 levels remained relatively consistent across all cell lines. Thus, patient fibroblasts may display a
202 compensatory adaptation to reduce the basal levels of BAX/BAK activation. Whether this
203 reduction in the ability to undergo apoptosis in response to mitochondrial stress is a widespread
204 phenomenon in all tissues of EMPF1 patients and/or whether apoptosis inhibition results in
205 deleterious accumulation of mitochondrial and nuclear DNA encoded mutations remains
206 unexplored. No significant alteration in the protein expression of DRP1 adaptors was detected
207 (Supplementary Fig. 2D)

208 **Mitochondrial hyperfusion in DRP1 mutant fibroblasts leads to higher glycolytic rate and**
209 **increased mitochondrial membrane potential**

210 Mitochondrial morphology is tightly linked to metabolic function (Wai & Langer, 2016; Dorn, 2015).
211 Thus, we assessed the effects of DRP1 patient mutations on cellular metabolism by measuring
212 rates of glycolysis and oxidative phosphorylation (OXPHOS) in cells using a Seahorse XF
213 Analyzer. The Seahorse analyzer measures extracellular oxygen consumption as a readout of
214 OXPHOS and extracellular acidification as a readout of glycolysis. Basal and maximal oxygen
215 consumption was not significantly different in mutant cells compared to control, suggesting no
216 major defects in ATP production (Fig. 3A). However, proton leak was significantly higher in the
217 G32A patient cells and coupling efficiency was significantly lower in both patient lines (Fig. 3B).
218 Therefore, although basal ATP production is not perturbed in the mutant cells, the electron
219 transport chain is not effectively coupling substrate oxidation and ATP synthesis. Extracellular
220 acidification rate was significantly increased in both patient lines, consistent with an upregulation
221 of glycolysis (Fig. 3A) and the hyperlactacidemia observed in more than 50% of patients with
222 mutations in DRP1 (Liu *et al*, 2021). A glycolytic rate assay confirmed that both basal and
223 compensatory glycolysis are higher in both patient lines (Fig. 3C). Thus, although the cells are

224 capable of producing ATP, DRP1 mutations cause a defect in OXPHOS efficiency and a
225 metabolic dependency on glycolysis (Fig. 3D).

226 The upregulation of glycolysis with no accompanied increase in oxidative phosphorylation led us
227 to interrogate a potential impairment in pyruvate transport. Two proteins are essential for
228 mitochondrial pyruvate transport in humans, Mitochondrial Pyruvate Carrier 1 and 2 (MPC1 and
229 MPC2) (Herzig *et al*, 2012; Bricker *et al*, 2012). MPC1 and MPC2 associate to form an ~150-
230 kilodalton complex in the inner mitochondrial membrane. We examined the expression of MPC1
231 and MPC2 using Western blot, which revealed a significant decrease in MPC2 expression in the
232 R403C cells (Fig. 3E). Real time quantitative PCR (RT-qPCR) gene expression analysis showed
233 a significant downregulation of *MPC2* expression in R403C cells and *MPC1* in both patient lines
234 (Fig. 3F). Taken together these data suggest that the upregulation in glycolysis seen in DRP1
235 mutant patient fibroblasts is a compensatory mechanism for impaired pyruvate import into the
236 mitochondria and/or decreased coupling efficiency of the ETC.

237 The major contributor of the proton motive force of the ETC is the mitochondrial membrane
238 potential, which drives oxidative phosphorylation. Thus, changes in OXPHOS coupling efficiency
239 can point to perturbation of the mitochondrial membrane potential and the maintenance of key ion
240 gradients. We investigated this possibility using the fluorescent sensor Tetramethylrhodamine,
241 ethyl ester (TMRE). TMRE is a cell-permeant, cationic, red-orange fluorescent dye that is
242 sequestered by polarized mitochondria. We found that mitochondrial membrane potential as
243 reported by TMRE was significantly increased in patient fibroblasts (Fig. 4), indicative of
244 hyperpolarization of the mitochondria.

245 **DRP1 mutations alter mitochondrial cristae morphology**

246 Cristae topology readjustments participate in energy balance control (Eramo *et al*, 2020; Kondadi
247 *et al*, 2020). The hyperpolarization of the mitochondrial membrane detected in patient fibroblasts

248 lead us to assess the effects of DRP1 mutations on cristae morphology. We used a previously
249 optimized method to quantify and analyze cristae morphology changes from transmission electron
250 microscopy (TEM) (Eisner *et al*, 2017; Lam *et al*, 2021). In this method, cristae abundance is
251 calculated by manually quantifying the number of cristae per mitochondrion, and a score between
252 0 (worst) and 4 (best) is assigned based on the morphology: (0—no well-defined cristae, 1—no
253 cristae in more than ~75% of the mitochondrial area, 2—no cristae in approximately ~25% of
254 mitochondrial area, 3—many cristae (over 75% of area) but irregular, 4—many regular cristae)
255 (Supplementary. Fig 3A). TEM of patient fibroblasts confirmed the mitochondrial elongation
256 observed in SIM (Supplementary Fig. 3B-D) and revealed differences in the cristae structure (Fig.
257 5A). The quantification of cristae morphology demonstrated a reduced cristae score and
258 decreased cristae number relative to mitochondrial length in DRP1-deficient cells compared with
259 the control cells (Fig. 5B). These data link aberrant outer mitochondrial membrane fission caused
260 by DRP1 mutations to generalized cristae structural changes. The structure and respiratory
261 function of mitochondrial cristae is maintained by the mitochondrial contact sites and cristae
262 organizing system (MICOS) complex – a large complex of scaffolding and membrane shaping
263 proteins localized at the inner mitochondrial membrane. Given the reduced cristae score, we
264 examined expression of some key components of the MICOS complex. *MIC19, MIC25,* and
265 *MIC60* are all reduced in either one or both patient lines at the mRNA level; however, protein
266 expression is not significantly changed (Supplementary. Fig. 4). The data suggest that the
267 structural abnormalities seen in patient fibroblasts are not due to changes in the expression of
268 proteins of the MICOS complex. Additional biochemical assays are needed to assess the
269 functionality of these proteins in the context of EMPF1.

270 **Patient fibroblasts display hyperfused peroxisomes**

271 In addition to catalyzing mitochondrial fission, DRP1 also participates in peroxisomal fission
272 (Kamerkar *et al*, 2018). While fission of peroxisomes has been demonstrated to be involved in *de*

273 *novo* peroxisomal biogenesis, the functional consequences of peroxisomal fission are not
274 completely understood. Previous reports using EMPF1 patient fibroblasts have not reported
275 elongation of peroxisomes, but DRP1 null cells have been reported to have hyperfused
276 peroxisomes (Kamerkar *et al*, 2018). To interrogate the effects of DRP1 mutations on peroxisome
277 morphology, we performed super-resolution microscopy. SIM revealed that both mutations in
278 DRP1 result in significant elongation of peroxisomes (Fig. 6A). Quantification of the peroxisome
279 structure shows an increase in volume, surface area, and length of peroxisomes (Fig. 6B). These
280 data confirm that DRP1 mutations found in patients with EMPF1 result in impaired peroxisome
281 fission.

282 Since peroxisomes and mitochondria are hubs for the regulation of fatty acid metabolism, we first
283 tested whether the dramatic changes in morphology would alter the expression of key genes
284 involved in fatty acid oxidation in patient fibroblasts. The expression of these genes have
285 previously been reported to increase in a DRP1 phosphomimetic mouse model (Valera-Alberni *et*
286 *al*, 2021). RT-qPCR analysis showed that the expression of carnitine palmitoyltransferase I,
287 *CPT1*, and acyl-coA dehydrogenase medium chain, *ACADM*, are significantly lower in patient
288 cells compared to control (Fig. 6C). CPT1 is associated with the outer mitochondrial membrane
289 and is responsible for catalyzing the transfer of the acyl group of acyl-CoA to L-carnitine. Fatty
290 acids are then able to move from the cytosol into the inner membrane space of the mitochondria
291 and the matrix, where fatty acid oxidation occurs. *ACADM* encodes for the medium-chain-acyl-
292 CoA dehydrogenase (MCAD) protein, which catalyzes the first step of mitochondrial fatty acid
293 beta-oxidation. Thus, the reduction in *CPT1* and *ACADM* expression may hinder the ability of the
294 mitochondria to carry out fatty acid oxidation.

295 To examine the ability of patient fibroblasts to perform fatty acid oxidation, we used the Seahorse
296 analyzer to quantify oxygen consumption rates of patient fibroblasts treated with either vehicle or
297 etomoxir, a CPT1 inhibitor. The cells were cultured with minimal glucose and glutamine and high

298 L-carnitine and palmitate to promote fatty acid oxidation over glycolysis or glutaminolysis. Control
299 fibroblasts treated with etomoxir show a reduction in maximal respiration following FCCP injection.
300 In contrast, the G32A patient-derived cells show no change in OCR with etomoxir treatment and
301 the R403C patient-derived cells show an increase in maximal respiration following FCCP injection
302 (Fig. 6D and Supplementary Fig. 5). These data indicate that, in contrast to the reliance of control
303 cells on long chain fatty acid oxidation under conditions of maximal respiration, both patient lines
304 have lost this dependency and adapted to the inhibition of long-chain fatty acid import into
305 mitochondria. These data show that fibroblasts with DRP1 mutations appear to have
306 compensatory adaptations to alterations in long-chain fatty acid oxidation.

307

308 **Discussion**

309 DRP1 is an essential gene for embryonic development (Wakabayashi *et al*, 2009; Ishihara *et al*,
310 2009). RNAi based approaches in human cell culture models have been used to explore the
311 impact of DRP1 loss on mitochondrial fission and downstream processes such as apoptosis and
312 mitophagy (Otera *et al*, 2016; Kleele *et al*, 2021; Smirnova *et al*, 2001). Although loss of DRP1
313 results in mitochondrial hyperfusion, it's not fully understood how mutations in DRP1 can impact
314 cellular metabolic function, cristae structure, and/or peroxisomal function. The analysis of
315 organelle morphology in fibroblast lines derived from patients with EMPF1 that harbor one wild-
316 type copy of DRP1 and one missense copy of DRP1, demonstrate a dominant negative effect of
317 mutant DRP1 that results in stalling of the fission machinery that has a wide impact on cellular
318 function.

319 Mitochondrial fission is essential for cellular processes such as apoptosis, mitophagy, and
320 mitochondrial biogenesis. However, how mitochondrial fission helps maintain cristae structure
321 and/or cellular metabolism has not been thoroughly explored. Our studies revealed that while
322 DRP1 is recruited to the mitochondria in EMPF1 patient lines, the fission event is incomplete, and
323 thus, mitochondrial fission is paused. This stalling of mitochondrial fission results in dramatic
324 changes to cristae morphology, notably a decrease in cristae score and number, indicative of
325 immature and poorly formed cristae. Changes in redox signaling can lead to cysteine oxidation of
326 MIC60 (Wasilewski & Chacinska, 2021; Li *et al*, 2021), an inner mitochondrial membrane protein
327 responsible for cristae structure integrity. Thus, the lack of proper mitochondrial fission in patient
328 cells may disrupt redox signaling, which may in turn be responsible for the aberrant cristae
329 morphology detected in patient cells.

330 Detailed metabolic analysis of patient fibroblasts showed that these cells have decreased
331 coupling efficiency and upregulation of glycolysis, suggesting that the functional impact of stalled
332 fission is electron transport chain inefficiency. This inefficiency may be due to the changes in

333 cristae structure, since cristae structure is essential for F_0F_1–ATPase to function effectively
334 (Wilkens *et al*, 2013; Afzal *et al*, 2021; Davies *et al*, 2011; Cogliati *et al*, 2013). Previous studies
335 revealed that there are distinct fission signatures that are key determinants of the decision of
336 mitochondria to proliferate or degrade (Kleele *et al*, 2021). Peripheral fission events were shown
337 to be preceded by a decrease in membrane potential and proton motive force. We found that the
338 elongated mitochondria from patient fibroblasts have a hyperpolarized membrane potential, which
339 could result from inefficient function of the F_0F_1–ATPase. Under certain conditions, the F_0F_1–
340 ATPase can pump protons out of the mitochondrial matrix into the intermembrane space in a
341 reverse-mode action, causing ΔΨm hyperpolarization. Alternatively, hyperpolarization may be
342 due to complex I inhibition or VDAC (voltage-dependent anion channel) opening, which can cause
343 hyperpolarization independently of F_0F_1–ATPase reverse-mode action (Forkink *et al*, 2014). A
344 comprehensive analysis of the functionality of the ETC complexes would be needed to elucidate
345 the connection between fission stalling events and mitochondrial hyperpolarization. Upregulation
346 of glycolysis in these patient fibroblasts could result in subsequent glucose depletion locally within
347 the cells, which could in turn cause ΔΨm hyperpolarization. Carbon-tracing could help reveal
348 whether all of the products of glycolysis are efficiently shuttled into the TCA cycle or if
349 intermediates are lost in the process. Investigating the function of uncoupling proteins such as
350 UCP2 and UCP3 may elucidate whether the decreased efficiency is a byproduct or cause of
351 mitochondrial dysfunction, such as increased ΔΨm, in these cells. Our finding that cells with
352 DRP1 mutations have profound alterations in cristae morphology but apparent maintenance of
353 overall ATP production, raises the interesting possibility that DRP1 mutant cells have evolved
354 specialized mechanisms to cope with electron leakage and damaging reactive oxygen species. A
355 landmark study from Spinelli and collaborators demonstrated the ability of complex II to work in
356 reverse in some tissues with the intrinsic capacity to use fumarate as a terminal electron acceptor
357 (Spinelli *et al*, 2021). It is plausible that complex II reversal has evolved as a mechanism to
358 maintain mitochondrial function in cells with alterations in fission caused by DRP1 mutations.

359 The existence of two mechanistically and functionally distinct types of fission at the mitochondria
360 and the peroxisomes have not been clearly elucidated. In our study, we demonstrate that patient
361 fibroblasts with mutations in DRP1 also have elongated peroxisomal morphology. Previous
362 studies in mammalian cell culture revealed that peroxisome membrane elongation precedes
363 membrane constriction and final membrane fission (Delille *et al*, 2010; Schrader *et al*, 2016).
364 Whether peroxisomes have a specialized fusion machinery is still under debate. However, we
365 speculate that under particular metabolic conditions peroxisomes, particularly those in contact
366 with mitochondria, may be able to fuse to respond to cellular metabolic needs. Elongation of the
367 peroxisomes in various human disorders has been associated with alterations in fatty acid
368 oxidation (Waterham *et al*, 2016). However; in these cells, peroxisomal function cannot be fully
369 dissociated from changes in mitochondrial morphology. Our model (Figure 7) suggests that the
370 mechanistic and functional connection between peroxisome remodeling and metabolic
371 homeostasis could be dysregulated in mitochondrial diseases such EMPF1. We propose that in
372 this context, human diseases could provide insight into the causal mechanisms underlying basic
373 cellular processes, such as organelle fission. The detailed elucidation of DRP1-centric
374 mechanisms will reveal the connection between organelle dynamics and cell fate. Several
375 questions remain: Does stalling of mitochondrial fission affect the association/dissociation of other
376 proteins at point of fission? Is peripheral fission also inhibited in patient fibroblasts? If that is the
377 case, what are the consequences for mitophagy and mitochondrial DNA integrity? What are the
378 effects of peroxisomal elongation on fatty acid metabolism? How is cell division and mitochondrial
379 segregation affected by DRP1 mutations? How are cell fate transitions affected by DRP1
380 mutations? Answering these fundamental questions would provide insight into the mechanisms
381 of mitochondrial fission under the lens of this rare disease caused by dysregulated mitochondrial
382 and peroxisomal homeostasis, and would inform the field on more rational and specific
383 therapeutic targets for these devastating neurodevelopmental disorders.

384 **STAR Methods**

385 **Cell Culture**

386 Human fibroblasts were thawed and plated directly in maintenance medium consisting of MEM
387 (Gibco #11095098) with 10% FBS (Sigma-Aldrich #F2442) and non-essential amino acids (Gibco
388 # 11-140-050). Cells were maintained at 37°C and 5% CO2 with media changes every other day.
389 Cells were passaged as needed using TrypLE (Thermo Fisher #12-064-013). For imaging
390 experiments, cells were re-plated onto #1.5 glass-bottom 35 mm dishes (Cellvis #D35C4-20-1.5-
391 N).

392 **Cell Treatments**

393 All treatments were added directly to fibroblasts in maintenance medium. The electron transport
394 chain decoupler CCCP (Sigma-Aldrich #C2759-250MG) was added to cells at a concentration of
395 1 μM. Cells were treated for 2 hours prior to fixation and imaging. All stock solutions were prepared
396 in DMSO.

397 **Plasmid Transfection**

398 Plasmid encoding mCherry-DRP1 (Addgene #49152) was transfected using FuGENE (Promega
399 #E2311) as described in the manufacturer protocol. Patient mutations were introduced to
400 plasmids using the In Fusion cloning kit (Takara Bio #638909) as described in the manufacturer
401 protocol. Cells were maintained until optimal transfection efficiency was reached before cells were
402 imaged.

403 **Immunofluorescence**

404 For immunofluorescence, cells were fixed with 4% paraformaldehyde for 20 min and
405 permeabilized in 1% Triton-X-100 for 10 min at room temperature. After blocking in 10% BSA,
406 cells were treated with primary and secondary antibodies using standard methods. Cells were
407 mounted in Fluoromount-G (Electron Microscopy Sciences #17984-25) prior to imaging. Primary

408 antibodies used include mouse anti-Mitochondria (Abcam #ab92824), rabbit anti-Tom20 (Cell
409 Signaling Technology #42406S), rabbit anti-DRP1 (Cell Signaling Technology #8570S), rabbit
410 anti-HSP60 (Cell Signaling Technologies # 12165S), mouse anti-PMP70 (Thermo Fisher # MA5-
411 31368), and rabbit anti-pDRP1 S616 (Cell Signaling Technology #3455S). Secondary antibodies
412 used include donkey anti-mouse Alexa Fluor-488 (Thermo Fisher Scientific #A21202), donkey
413 anti-rabbit Alexa Fluor-488 (Thermo Fisher Scientific #A21206), and donkey anti-mouse Alexa
414 Fluor-546 (Thermo Fisher Scientific #A10036), and donkey anti-rabbit Alexa Fluor-546 (Thermo
415 Fisher Scientific #A10040).

416 **Western Blot**

417 Gel samples were prepared by mixing cell lysates with LDS sample buffer (Life Technologies,
418 #NP0007) and 2-Mercaptoethanol (BioRad #1610710) and boiled at 95°C for 5 minutes. Samples
419 were resolved on 4-20% Mini-PROTEAN TGX precast gels (BioRad #4561096) and transferred
420 onto PVDF membrane (BioRad #1620177). Antibodies used for Western blotting are as follows:
421 rabbit anti-DRP-1 (Cell Signaling Technologies #8570S), rabbit anti-pDRP-1 S616 (Cell Signaling
422 Technologies #3455S), rabbit anti-OPA1 (Cell Signaling Technologies #67589S), mouse anti-
423 MFN1 (Abcam #ab57602, mouse anti-MFN2 (Abcam #ab56889), rabbit anti-MFF (Proteintech
424 #17090-1-AP), rabbit anti-MiD49 (Proteintech #16413-1-AP), rabbit anti-MiD51 (Proteintech
425 #20164-1-AP), and rabbit anti-FIS1 (Proteintech #10956-1-AP), and mouse anti-HSP70
426 (Invitrogen #MA3-006).

427 **Seahorse XF Analysis**

428 Fibroblasts were plated onto Seahorse XF96 V3 PS cell culture microplates 2 days before the
429 assay at 50,000 cells per well. One hour prior to the assay, media was switched to XF DMEM
430 media containing 1 mM pyruvate, 2 mM glutamine, and 10 mM glucose. For the Seahorse XF
431 Mito Stress Test, oxygen consumption rate (OCR) was measured sequentially after addition of
432 1.0 μM oligomycin, 0.5 μM FCCP, and 0.5 μM rotenone plus Antimycin A. Protein leak and

433 coupling efficiency were calculated using OCR. For the Seahorse XF Glycolytic Rate Assay, basal
434 glycolytic rate was measured by extracellular acidification, and compensatory glycolysis was
435 measured after addition of 0.5 μM rotenone plus antimycin A. Treatment with 50 mM 2-DG was
436 used as a negative control. For the Seahorse XF Fuel Flex Test, glutamine dependency was
437 measured by sequential addition of 3.0 μM BPTES followed by 4.0 μM Etomoxir plus 2.0 μM
438 UK5099. Fatty acid dependency was measured by sequential addition of 4.0 μM Etomoxir
439 followed by 3.0 μM BPTES plus 2.0 μM UK5099. Glucose dependency was measured by
440 sequential addition of 2.0 μM UK5099 followed by 3.0 μM BPTES plus 4.0 μM Etomoxir. For the
441 Seahorse XF Long Chain Fatty Acid Oxidation Stress Test, 24 hours prior to assay cells were
442 switched to base media containing 0.5 mM glucose, 1.0 mM glutamine, 0.5 mM XF L-carnitine,
443 and 1.0 % fetal bovine serum. One hour prior to the assay, media was switched to XF DMEM
444 media containing 2 mM glucose, 0.5 mM L-Carnitine, and Palmitate-BSA. Oxygen consumption
445 rate (OCR) was measured sequentially after addition of 4.0 μM etomoxir, 1.5 μM oligomycin, 2.0
446 μM FCCP, and 0.5 μM rotenone plus Antimycin A.

447 **RNA Extraction and cDNA Synthesis**

448 Cells were washed with PBS and scraped into 1000μl Trizol reagent. 200μl of chloroform was
449 added and the samples were incubated at room temperature for 5 minutes. The samples were
450 spun down at 12,000 g and the aqueous phase was collected. 500μl of isopropanol was added
451 to precipitate RNA and the sample was incubated for 25 minutes at room temperature, followed
452 by centrifugation at 12,000 g for 10 min at 4°C. The RNA pellet was washed with 75% ethanol,
453 semi-dried, and resuspended in 30μl of DEPC water. After quantification and adjusting the volume
454 of all the samples to 1μg/μl, the samples were treated with DNAse (New England Biolabs, #
455 M0303). 10μl of this volume was used to generate cDNA using the manufacturer's protocol
456 (Thermo Fisher, #4368814).

457 **Quantitative RT PCR (RT-qPCR)**

458 1ug of cDNA sample was used to run RT-qPCR for the primers mentioned in the table.
459 QuantStudio 3 Real-Time PCR machine, SYBR green master mix (Thermo Fisher, #4364346),
460 and manufacturer instructions were used to set up the assay.

461 **Image Acquisition**

462 Super-resolution images were acquired using a Nikon SIM microscope equipped with a 1.49 NA
463 100x Oil objective an Andor DU-897 EMCCD camera. Live-imaging experiments experiments
464 were acquired on a Nikon Eclipse Ti-E spinning disk confocal microscope equipped with a 1.40
465 NA 60X Oil objective and an Andor DU-897 EMCCD camera. Image processing and quantification
466 was performed using Fiji.

467 **Sample Preparation for Transmission Electron Microscope (TEM) Analysis**

468 Human fibroblasts were immediately washed in ice-cold saline. Samples were processed as
469 described by (Lam et. al., 2021, Pereira et al., 2017). Cells were fixed in 2.5% glutaraldehyde in
470 sodium cacodylate buffer for 1 hour at 37 °C, embedded in 2% agarose, postfixed in buffered 1%
471 osmium tetroxide, stained in 2% uranyl acetate, and dehydrated with an ethanol graded series.
472 After embedding in EMbed-812 resin, 80 nm sections were cut on an ultramicrotome and stained
473 with 2% uranyl acetate and lead citrate. Images were acquired on a JEOL JEM-1230
474 Transmission Electron Microscope, operating at 120 kV. Random images of human fibroblasts
475 were obtained.

476 **TEM Analysis**

477 Measurements of mitochondrial area, circularity, and length were performed using the multi-
478 measure region of interest (ROI) tool in ImageJ (Lam et. al., 2021, Parra et al., 2014). To measure
479 cristae morphology, we used ROIs in ImageJ to determine the cristae area, circulatory index,
480 number, volume, and cristae score. The NIH ImageJ software was used to manually trace and
481 analyze all mitochondria or cristae using the freehand told in the ImageJ application (Lam et. al.,

482 2021, Parra et al., 2014). To assign a mitochondrion a cristae score, cristae abundance and form
483 were evaluated. A score between 0 and 4 (0 – no sharply defined crista, 1 – greater than 50% of
484 mitochondrial area without cristae, 2 – greater than 25% of mitochondrial area without cristae, 3
485 – many cristae but irregular, 4 – many regular cristae) was assigned (Eisner *et al*, 2017).

486 **Serial Block Facing-Scanning Electron Microscopy (SBF-SEM) Processing**

487 Human fibroblasts were fixed in 2% glutaraldehyde in 0.1 M cacodylate buffer and processed
488 using a heavy metal protocol adapted from a previously published protocol (Courson et al., 2021;
489 Mustafi et al., 2014). Human fibroblasts were immersed in 3% potassium ferrocyanide and 2%
490 osmium tetroxide (1 hour at 4 °C), followed by filtered 0.1% thiocarbohydrazide (20 min), 2%
491 osmium tetroxide (30 min), and left overnight in 1% uranyl acetate at 4 °C (several de-ionized
492 H2O washes were performed between each step). The next day samples were immersed in a
493 0.6% lead aspartate solution (30 min at 60 °C and dehydrated in graded acetone (as described
494 for TEM). Human fibroblasts were impregnated with epoxy Taab 812 hard resin, embedded in
495 fresh resin, and polymerized at 60 °C for 36–48 hours. After polymerization, the block was
496 sectioned for TEM to identify the area of interest, then trimmed to 0.5 mm × 0.5 mm and glued to
497 an aluminum pin. The pin was placed into an FEI/Thermo Scientific Volumescope 2 scanning
498 electron microscope (SEM). The scope is a state-of-the-art SBF imaging system. For 3D EM
499 reconstruction, thin (0.09 μm) serial sections, 300 to 400 per block, were obtained from the blocks
500 that were processed for conventional TEM. Serial sections were collected onto formvar coated
501 slot grids (Pella, Redding CA), stained, and imaged, as described above. The segmentation of
502 SBF-SEM reconstructions was performed by manually tracing structural features through
503 sequential slices of the micrograph block. Images were collected from 30–50 serial sections,
504 which were then stacked, aligned, and visualized using Amira to make videos and quantify
505 volumetric structures.

506 **Statistical Analysis**

507 All experiments were performed with a minimum of 3 biological replicates. Statistical significance
508 was determined by one-way or repeated measures ANOVA as appropriate for each experiment.
509 GraphPad Prism v8.1.2 was used for all statistical analysis and data visualization. Error bars in
510 all bar graphs represent standard error of the mean unless otherwise noted in the figure. No
511 outliers were removed from the analyses. Quantification of mitochondrial morphology was
512 performed in NIS-Elements (Nikon); briefly, we segmented mitochondria in 3D and performed
513 skeletonization of the resulting 3D mask. Skeleton major axis length, volume, and surface area
514 measurements were exported into Excel. For EM, the results are presented as the mean ±
515 standard error of the mean. Data were analyzed using an unpaired T-test. If more than two groups
516 were compared, one-way analysis of variance (ANOVA) was performed, and significance was
517 assessed using Fisher's protected least significance difference test. GraphPad PRISM and
518 Statplus software package was used for t-tests and ANOVA analyses (SAS Institute: Cary, NC,
519 USA). For all statistical analyses, a significant difference was accepted when $P < 0.05$.

520 **Acknowledgements**

521 We would like to thank the patients and families for permission to publish this work. We thank Dr.
522 Eric Payne and Dr. Suzanne Hoppins for providing the patient-derived fibroblast lines used in this
523 paper. We would also like to thank Dr. Evan Krystofiak for providing EM expertise, and Dr.
524 Matthew Tyska, Dr. Uri Manor, and Dr. Kari Seedle, for providing advice and expertise with high-
525 resolution microscopy. This work was supported by 1R35 GM128915-01NIGMS (VG),
526 1RF1MH123971-01 (VG); the Precision Medicine and Mental Health Initiative sponsored by the
527 Vanderbilt Brain Institute (VG), 1R21CA227483-01A1NCI (VG), F99NS125829 (GLR), HHMI
528 Gilliam (GLR), and CBMS T32 (GLR). All SIM and spinning disk confocal microscopy imaging
529 and image analysis were performed in part through the use of the Vanderbilt Cell Imaging Shared
530 Resource, which is supported by NIH grants 1S10OD012324-01 and 1S10OD021630-01. The
531 authors declare no competing financial interests.

532 **Author Contributions**

533 G. Robertson and V. Gama conceived the study, designed experiments, interpreted data, and
534 wrote the manuscript. G. Robertson designed and carried out all the cell biology experiments,
535 with technical assistance from M. Patel and S. Riffle. J. Mears provided technical feedback and
536 insight into the conception and execution of study. A. Marshall, H. Beasley, Z. Vue, J. Shao, and
537 E. Garza Lopez performed the TEM, 3D EM and sbf-SEM experiments, quantification, and
538 analysis, supervised by A. Hinton.

539 **Figure Legends**

540 **Figure 1. DRP1 patient-derived fibroblasts have elongated mitochondrial morphology.** (A)
541 Representative images of mitochondrial morphology in patient-derived fibroblasts using
542 structured illumination microscopy (n=3, 7 cells per replicate). Scale bar: 5 μm. (B) Quantification
543 of mitochondrial volume, surface area, and major axis length. Analyzed using one-way ANOVA
544 followed by Dunnett's multiple comparison test. (C) Representative sbf-SEM 3D reconstructed
545 images. Each mitochondrion is colored a unique color. (D) Quantification of sbf-SEM for 3D
546 mitochondrial length, volume, and complexity index. Analyzed using one-way ANOVA followed
547 by Dunnett's multiple comparison test. (E) Representative images of mitochondrial morphology in
548 control fibroblasts transfected with either $DRP1^{WT}$-mCherry, $DRP1^{G32A}$-mCherry, or $DRP1^{R403C}$-
549 mCherry using structured illumination microscopy (n=3, 7 cells per replicate). Top scale bar: 1
550 μm. Bottom scale bar: 5 μm. (F) Quantification of mitochondrial volume, surface area, and major
551 axis length. Analyzed using one-way ANOVA followed by Dunnett's multiple comparison test.

552 **Figure 2. Mutant G32A and R403C DRP1 are recruited to mitochondria. i.** (A) Western blot of
553 total protein lysate isolated from patient fibroblasts and probed for mitochondrial fusion proteins.
554 Representative image of three independent biological replicates. (B) Western blot of total protein
555 lysate isolated from patient fibroblasts and probed for mitochondrial fission proteins. Band density
556 is normalized to loading control (HSP70) and relative to control cells. Representative image of

557 three independent biological replicates. (C) Representative images of mitochondrial and DRP1 in
558 patient-derived fibroblasts using structured illumination microscopy (n=3, 7 cells per replicate).
559 Scale bar: 5 μm. Top image is a zoom of white box from bottom image. Scale bar: 1 μm. (D)
560 Quantification of DRP1 puncta that overlap with mitochondria and volume of DRP1 puncta.
561 Analyzed using one-way ANOVA followed by Dunnett's multiple comparison test. (E)
562 Representative images of mitochondrial morphology in patient-derived fibroblasts treated with
563 either DMSO or CCCP for 1 hours using structured illumination microscopy (n=3, 7 cells per
564 replicate). Scale bar: 5 μm. (F) Quantification of mitochondrial volume, surface area, and major
565 axis length. Analyzed using one-way ANOVA followed by Dunnett's multiple comparison test.

566 **Figure 3. Mitochondrial defects lead to inefficient coupling of the electron transport chain**
567 **and higher glycolytic rate.** (A) Oxygen consumption rate and extracellular acidification rate in
568 patient fibroblasts as measured using Seahorse Mitochondrial stress test (n=3, 20 wells per
569 replicate). Oligomycin applied at 20 minutes, FCCP applied at 40 minutes, and
570 rotenone/Antimycin A applied at 60 minutes. Analyzed using two-way ANOVA followed by Šídák's
571 multiple comparisons test. (B) Proton leak and coupling efficiency calculated using oxygen
572 consumption rate. (C) Basal glycolysis of patient fibroblasts measure using Seahorse Glycolytic
573 Rate Assay. Compensatory glycolysis measured following application of rotenone/Antimycin A.
574 (D) Glucose, glutamine, and fatty acid dependency of the electron transport chain measured using
575 Seahorse Fuel Flex Assay. Glucose dependency measured after application of UK5099,
576 glutamine dependency measured after application of BPTES, and fatty acid dependency measure
577 after application of Etomoxir. (E) qRT-PCR analysis of gene expression in fibroblasts relative to
578 control and normalized to two housekeeping genes (*GPI* and *GAPDH)*. Quantifications are shown
579 for three independent biological replicates. (F) Western blot of total protein lysate isolated from
580 patient fibroblasts and probed for mitochondrial pyruvate carriers. Band density is normalized to

581 loading control (HSP70) and relative to control cells. Representative image of three independent
582 biological replicates.

583 **Figure 4. DRP1 patient fibroblasts have more hyperpolarized mitochondrial membrane**
584 **potential.** (A) Representative live-cell imaging of patient-derived fibroblasts treated with 500nM
585 TMRE for 10 minutes. Cells were imaged every 15 seconds for 15 minutes using spinning disk
586 confocal (n=3, 7 cells per replicate). Scale bar: 5 μm.

587 **Figure 5. Cristae morphology is altered in patient cells.** (A) Transmission electron microscopy
588 of patient fibroblasts. 3 representative images per line shown. (B) Quantification of cristae from
589 TEM images for cristae score and cristae number relative to mitochondrial length. Analyzed using
590 one-way ANOVA followed by Dunnett's multiple comparison test.

591 **Figure 6. Patient fibroblasts have elongated peroxisomes.** (A) Representative images of
592 peroxisomal morphology in patient-derived fibroblasts using structured illumination microscopy
593 (n=3, 7 cells per replicate). Scale bar: 5 μm. Bottom image is a zoom from top image. (B)
594 Quantification of peroxisomal volume, surface area, and major axis length. Analyzed using one-
595 way ANOVA followed by Dunnett's multiple comparison test. (C) qRT-PCR analysis of gene
596 expression in fibroblasts relative to control and normalized to two housekeeping genes (*GPI* and
597 *GAPDH)*. Quantifications are shown for three independent biological replicates. (D) Oxygen
598 consumption rate in patient fibroblasts as measured using Seahorse Analyzer XFe96 (n=3, 20
599 wells per replicate). Etomoxir applied after 20 minutes, oligomycin applied at 40 minutes, FCCP
600 applied at 60 minutes, and rotenone/Antimycin A applied at 80 minutes. Analyzed using two-way
601 ANOVA followed by Šídák's multiple comparisons test.

602 **Figure 7: Current model of the cellular responses to EMPF1 associated DRP1 mutations.**
603 EMPF1- associated mutations do not appear to alter the capacity of DRP1 to be recruited to points
604 of fission, but rather cause stalling of the fission events. Pausing peroxisomal and mitochondrial

605 fission results in alterations of cristae structure, changes in mitochondrial membrane potential,
606 decreased mitochondrial coupling efficiency, delayed cell death response, and overall metabolic
607 adaptations.

608 **References**

609 Afzal N, Lederer WJ, Jafri MS & Mannella CA (2021) Effect of crista morphology on mitochondrial
610 ATP output: A computational study. *Curr Res Physiol* 4: 163–176

611 Alexander C, Votruba M, Pesch UEA, Thiselton DL, Mayer S, Moore A, Rodriguez M, Kellner U,
612 Leo-Kottler B, Auburger G, *et al* (2000) OPA1, encoding a dynamin-related GTPase, is
613 mutated in autosomal dominant optic atrophy linked to chromosome 3q28. *Nat Genet 2000*
614 *262* 26: 211–215

615 Bayraktar EC, Baudrier L, Özerdem C, Lewis CA, Chan SH, Kunchok T, Abu-Remaileh M,
616 Cangelosi AL, Sabatini DM, Birsoy K, *et al* (2019) MITO-Tag Mice enable rapid isolation and
617 multimodal profiling of mitochondria from specific cell types in vivo. *Proc Natl Acad Sci U S*
618 *A* 116: 303–312

619 Bricker DK, Taylor EB, Schell JC, Orsak T, Boutron A, Chen YC, Cox JE, Cardon CM, Van
620 Vranken JG, Dephoure N, *et al* (2012) A mitochondrial pyruvate carrier required for pyruvate
621 uptake in yeast, Drosophila, and humans. *Science* 337: 96–100

622 Chakrabarti R, Ji WK, Stan R V., Sanz J de J, Ryan TA & Higgs HN (2018) INF2-mediated actin
623 polymerization at the ER stimulates mitochondrial calcium uptake, inner membrane
624 constriction, and division. *J Cell Biol* 217: 251–268

625 Chandel NS (2021) Lipid Metabolism. *Cold Spring Harb Perspect Biol* 13

626 Chang C & Blackstone C (2007) Drp1 phosphorylation and mitochondrial regulation. *EMBO Rep*
627 8: 1088–1089

628 Chao YH, Robak LA, Xia F, Koenig MK, Adesina A, Bacino CA, Scaglia F, Bellen HJ & Wangler
629 MF (2016) Missense variants in the middle domain of DNM1L in cases of infantile
630 encephalopathy alter peroxisomes and mitochondria when assayed in Drosophila. *Hum Mol*

631 *Genet* 25: 1846–1856

632 Chen H, Detmer SA, Ewald AJ, Griffin EE, Fraser SE & Chan DC (2003) Mitofusins Mfn1 and
633 Mfn2 coordinately regulate mitochondrial fusion and are essential for embryonic
634 development. *J Cell Biol* 160: 189–200

635 Cogliati S, Frezza C, Soriano ME, Varanita T, Quintana-Cabrera R, Corrado M, Cipolat S, Costa
636 V, Casarin A, Gomes LC, *et al* (2013) Mitochondrial Cristae Shape Determines Respiratory
637 Chain Supercomplexes Assembly and Respiratory Efficiency. *Cell* 155: 160–171

638 Csordás G, Renken C, Várnai P, Walter L, Weaver D, Buttle KF, Balla T, Mannella CA &
639 Hajnóczky G (2006) Structural and functional features and significance of the physical
640 linkage between ER and mitochondria. *J Cell Biol* 174: 915–921

641 Davies KM, Strauss M, Daum B, Kief JH, Osiewacz HD, Rycovska A, Zickermann V & Kühlbrandt
642 W (2011) Macromolecular organization of ATP synthase and complex I in whole
643 mitochondria. *Proc Natl Acad Sci U S A* 108: 14121–14126

644 Delettre C, Lenaers G, Griffoin JM, Gigarel N, Lorenzo C, Belenguer P, Pelloquin L, Grosgeorge
645 J, Turc-Carel C, Perret E, *et al* (2000) Nuclear gene OPA1, encoding a mitochondrial
646 dynamin-related protein, is mutated in dominant optic atrophy. *Nat Genet 2000 262* 26: 207–
647 210

648 Delille HK, Agricola B, Guimaraes SC, Borta H, Lüers GH, Fransen M & Schrader M (2010)
649 Pex11pbeta-mediated growth and division of mammalian peroxisomes follows a maturation
650 pathway. *J Cell Sci* 123: 2750–2762

651 Ding L, Sun W, Balaz M, He A, Klug M, Wieland S, Caiazzo R, Raverdy V, Pattou F, Lefebvre P,
652 *et al* (2021) Peroxisomal β-oxidation acts as a sensor for intracellular fatty acids and
653 regulates lipolysis. *Nat Metab* 3: 1648–1661

654 Dorn GW (2015) Mitochondrial dynamism and heart disease: changing shape and shaping
655 change. *EMBO Mol Med* 7: 865–877

656 Eisner V, Cupo RR, Gao E, Csordás G, Slovinsky WS, Paillard M, Cheng L, Ibetti J, Chen SRW,
657 Chuprun JK, *et al* (2017) Mitochondrial fusion dynamics is robust in the heart and depends
658 on calcium oscillations and contractile activity. *Proc Natl Acad Sci U S A* 114: E859–E868

659 Eramo MJ, Lisnyak V, Formosa LE & Ryan MT (2020) The 'mitochondrial contact site and cristae
660 organising system' (MICOS) in health and human disease. *J Biochem* 167: 243–255

661 Fahrner JA, Liu R, Perry MS, Klein J & Chan DC (2016) A novel de novo dominant negative
662 mutation in DNM1L impairs mitochondrial fission and presents as childhood epileptic
663 encephalopathy. *Am J Med Genet A* 170: 2002–2011

664 Faitg J, Lacefield C, Davey T, White K, Laws R, Kosmidis S, Reeve AK, Kandel ER, Vincent AE
665 & Picard M (2021) 3D neuronal mitochondrial morphology in axons, dendrites, and somata
666 of the aging mouse hippocampus. *Cell Rep* 36

667 Fan J, Li X, Issop L, Culty M & Papadopoulos V (2016) ACBD2/ECI2-Mediated Peroxisome-
668 Mitochondria Interactions in Leydig Cell Steroid Biosynthesis. *Mol Endocrinol* 30: 763–782

669 Ferreira AR, Marques M, Ramos B, Kagan JC & Ribeiro D (2021) Emerging roles of peroxisomes
670 in viral infections. *Trends Cell Biol*

671 Fonseca TB, Sánchez-Guerrero Á, Milosevic I & Raimundo N (2019) Mitochondrial fission
672 requires DRP1 but not dynamins. *Nature* 570: E34–E42 doi:10.1038/s41586-019-1296-y
673 [PREPRINT]

674 Forkink M, Manjeri GR, Liemburg-Apers DC, Nibbeling E, Blanchard M, Wojtala A, Smeitink JAM,
675 Wieckowski MR, Willems PHGM & Koopman WJH (2014) Mitochondrial hyperpolarization
676 during chronic complex I inhibition is sustained by low activity of complex II, III, IV and V.

677 *Biochim Biophys Acta - Bioenerg* 1837: 1247–1256

678 Francy CA, Alvarez FJD, Zhou L, Ramachandran R & Mears JA (2015) The Mechanoenzymatic
679 Core of Dynamin-related Protein 1 Comprises the Minimal Machinery Required for
680 Membrane Constriction *. *J Biol Chem* 290: 11692–11703

681 Fransen M, Lismont C & Walton P (2017) The Peroxisome-Mitochondria Connection: How and
682 Why? *Int J Mol Sci* 18

683 Friedman JR, Lackner LL, West M, DiBenedetto JR, Nunnari J & Voeltz GK (2011) ER tubules
684 mark sites of mitochondrial division. *Science (80-)* 334: 358–362

685 Fröhlich C, Grabiger S, Schwefel D, Faelber K, Rosenbaum E, Mears J, Rocks O & Daumke O
686 (2013) Structural insights into oligomerization and mitochondrial remodelling of dynamin 1-
687 like protein. *EMBO J* 32: 1280–1292

688 Gandre-Babbe S & Van Der Bliek AM (2008) The novel tail-anchored membrane protein Mff
689 controls mitochondrial and peroxisomal fission in mammalian cells. *Mol Biol Cell* 19: 2402–
690 2412

691 Garza-Lopez E, Vue Z, Katti P, Neikirk K, Biete M, Lam J, Beasley HK, Marshall AG, Rodman
692 TA, Christensen TA, *et al* (2021) Protocols for Generating Surfaces and Measuring 3D
693 Organelle Morphology Using Amira. *Cells 2022, Vol 11, Page 65* 11: 65

694 Hatch AL, Gurel PS & Higgs HN (2014) Novel roles for actin in mitochondrial fission. *J Cell Sci*
695 127: 4549–4560

696 Hatch AL, Ji WK, Merrill RA, Strack S & Higgs HN (2016) Actin filaments as dynamic reservoirs
697 for Drp1 recruitment. *Mol Biol Cell* 27: 3109–3121

698 Herzig S, Raemy E, Montessuit S, Veuthey JL, Zamboni N, Westermann B, Kunji ERS & Martinou
699 JC (2012) Identification and functional expression of the mitochondrial pyruvate carrier.

700 *Science* 337: 93–96

701 Ishihara N, Nomura M, Jofuku A, Kato H, Suzuki SO, Masuda K, Otera H, Nakanishi Y, Nonaka
702 I, Goto YI, *et al* (2009) Mitochondrial fission factor Drp1 is essential for embryonic
703 development and synapse formation in mice. *Nat Cell Biol* 11: 958–966

704 Itoyama A, Michiyuki S, Honsho M, Yamamoto T, Moser A, Yoshida Y & Fujiki Y (2013) Mff
705 functions with Pex11pβ and DLP1 in peroxisomal fission. *Biol Open* 2: 998

706 Iwata R, Casimir P & Vanderhaeghen P (2020) Mitochondrial dynamics in postmitotic cells
707 regulate neurogenesis. *Science (80-)* 369: 858–862

708 Ji WK, Chakrabarti R, Fan X, Schoenfeld L, Strack S & Higgs HN (2017) Receptor-mediated Drp1
709 oligomerization on endoplasmic reticulum. *J Cell Biol* 216: 4123–4139

710 Ji WK, Hatch AL, Merrill RA, Strack S & Higgs HN (2015) Actin filaments target the oligomeric
711 maturation of the dynamin GTPase Drp1 to mitochondrial fission sites. *Elife* 4

712 Kamerkar SC, Kraus F, Sharpe AJ, Pucadyil TJ & Ryan MT (2018) Dynamin-related protein 1 has
713 membrane constricting and severing abilities sufficient for mitochondrial and peroxisomal
714 fission. *Nat Commun* 9: 1–15

715 Keller N, Paketci C, Edem P, Thiele H, Yis U, Wirth B & Karakaya M (2021) De novo DNM1L
716 variant presenting with severe muscular atrophy, dystonia and sensory neuropathy. *Eur J*
717 *Med Genet* 64

718 Khacho M, Clark A, Svoboda DS, Azzi J, MacLaurin JG, Meghaizel C, Sesaki H, Lagace DC,
719 Germain M, Harper ME, *et al* (2016) Mitochondrial Dynamics Impacts Stem Cell Identity and
720 Fate Decisions by Regulating a Nuclear Transcriptional Program. *Cell Stem Cell* 19: 232–
721 247

722 King WT, Axelrod CL, Zunica ERM, Noland RC, Davuluri G, Fujioka H, Tandler B, Pergola K,

723 Hermann GE, Rogers RC, *et al* (2021) Dynamin-related protein 1 regulates substrate
724 oxidation in skeletal muscle by stabilizing cellular and mitochondrial calcium dynamics. *J Biol*
725 *Chem* 297: 101196

726 Kleele T, Rey T, Winter J, Zaganelli S, Mahecic D, Perreten Lambert H, Ruberto FP, Nemir M,
727 Wai T, Pedrazzini T, *et al* (2021) Distinct fission signatures predict mitochondrial degradation
728 or biogenesis. *Nature* 593: 435–439

729 Koch A, Thiemann M, Grabenbauer M, Yoon Y, McNiven MA & Schrader M (2003) Dynamin-like
730 protein 1 is involved in peroxisomal fission. *J Biol Chem* 278: 8597–8605

731 Koch J & Brocard C (2012) PEX11 proteins attract Mff and human Fis1 to coordinate peroxisomal
732 fission. *J Cell Sci* 125: 3813–3826

733 Kondadi AK, Anand R, Hänsch S, Urbach J, Zobel T, Wolf DM, Segawa M, Liesa M, Shirihai OS,
734 Weidtkamp-Peters S, *et al* (2020) Cristae undergo continuous cycles of membrane
735 remodelling in a MICOS-dependent manner. *EMBO Rep* 21: e49776

736 Lam J, Katti P, Biete M, Mungai M, Ashshareef S, Neikirk K, Lopez EG, Vue Z, Christensen TA,
737 Beasley HK, *et al* (2021) A Universal Approach to Analyzing Transmission Electron
738 Microscopy with ImageJ. *Cells 2021, Vol 10, Page 2177* 10: 2177

739 Lee YJ, Jeong SY, Karbowski M, Smith CL & Youle RJ (2004) Roles of the mammalian
740 mitochondrial fission and fusion mediators Fis1, Drp1, and Opa1 in apoptosis. *Mol Biol Cell*
741 15: 5001–5011

742 Lewis SC, Uchiyama LF & Nunnari J (2016) ER-mitochondria contacts couple mtDNA synthesis
743 with Mitochondrial division in human cells. *Science (80-)* 353

744 Li L, Conradson DM, Bharat V, Kim MJ, Hsieh CH, Minhas PS, Papakyrikos AM, Durairaj AS,
745 Ludlam A, Andreasson KI, *et al* (2021) A mitochondrial membrane-bridging machinery

746 mediates signal transduction of intramitochondrial oxidation. *Nat Metab* 3: 1242–1258

747 Li S, Xu S, Roelofs BA, Boyman L, Jonathan Lederer W, Sesaki H & Karbowski M (2015)
748 Transient assembly of F-actin on the outer mitochondrial membrane contributes to
749 mitochondrial fission. *J Cell Biol* 208: 109–123

750 Liu X, Zhang Z, Li D, Lei M, Li Q, Liu X & Zhang P (2021) DNM1L-Related Mitochondrial Fission
751 Defects Presenting as Encephalopathy: A Case Report and Literature Review. *Front Pediatr*
752 9

753 Lodhi IJ & Semenkovich CF (2014) Peroxisomes: a nexus for lipid metabolism and cellular
754 signaling. *Cell Metab* 19: 380–392

755 Longo F, Benedetti S, Zambon AA, Sora MGN, Di Resta C, De Ritis D, Quattrini A, Maltecca F,
756 Ferrari M & Previtali SC (2020) Impaired turnover of hyperfused mitochondria in severe
757 axonal neuropathy due to a novel DRP1 mutation. *Hum Mol Genet* 29: 177–188

758 Losó n OC, Song Z, Chen H & Chan DC (2013) Fis1, Mff, MiD49, and MiD51 mediate Drp1
759 recruitment in mitochondrial fission. *Mol Biol Cell* 24: 659–667

760 Martinou JC & Youle RJ (2006) Which came first, the cytochrome c release or the mitochondrial
761 fission? *Cell Death Differ* 13: 1291–1295

762 Montecinos-Franjola F, Bauer BL, Mears JA & Ramachandran R (2020) GFP fluorescence
763 tagging alters dynamin-related protein 1 oligomerization dynamics and creates disassembly-
764 refractory puncta to mediate mitochondrial fission. *Sci Reports 2020 101* 10: 1–16

765 Nagashima S, Tábara LC, Tilokani L, Paupe V, Anand H, Pogson JH, Zunino R, McBride HM &
766 Prudent J (2020) Golgi-derived PI(4)P-containing vesicles drive late steps of mitochondrial
767 division. *Science (80-)* 367: 1366–1371

768 Nasca A, Legati A, Baruffini E, Nolli C, Moroni I, Ardissone A, Goffrini P & Ghezzi D (2016) Biallelic

769 Mutations in DNM1L are Associated with a Slowly Progressive Infantile Encephalopathy.
770 *Hum Mutat* 37: 898–903

771 Nolan DA, Chen B, Michon AM, Salatka E & Arndt D (2019) A Rasmussen encephalitis,
772 autoimmune encephalitis, and mitochondrial disease mimicker: expanding the *DNM1L*-
773 associated intractable epilepsy and encephalopathy phenotype. *Epileptic Disord* 21: 112–
774 116

775 Osellame LD, Singh AP, Stroud DA, Palmer CS, Stojanovski D, Ramachandran R & Ryan MT
776 (2016) Cooperative and independent roles of the Drp1 adaptors Mff, MiD49 and MiD51 in
777 mitochondrial fission. *J Cell Sci* 129: 2170–2181

778 Otera H, Miyata N, Kuge O & Mihara K (2016) Drp1-dependent mitochondrial fission via MiD49/51
779 is essential for apoptotic cristae remodeling. *J Cell Biol* 212: 531–544

780 Palmer CS, Elgass KD, Parton RG, Osellame LD, Stojanovski D & Ryan MT (2013) Adaptor
781 proteins MiD49 and MiD51 can act independently of Mff and Fis1 in Drp1 recruitment and
782 are specific for mitochondrial fission. *J Biol Chem* 288: 27584–27593

783 Prigione A & Adjaye J (2011) Modulation of mitochondrial biogenesis and bioenergetic
784 metabolism upon in vitro and in vivo differentiation of human ES and iPS cells. *Int J Dev Biol*
785 54: 1729–1741 doi:10.1387/ijdb.103198ap [PREPRINT]

786 Rasmussen ML, Taneja N, Neininger AC, Wang L, Robertson GL, Riffle SN, Shi L, Knollmann
787 BC, Burnette DT & Gama V (2020) MCL-1 Inhibition by Selective BH3 Mimetics Disrupts
788 Mitochondrial Dynamics Causing Loss of Viability and Functionality of Human
789 Cardiomyocytes. *iScience* 23

790 Ravi A, Palamiuc L, Loughran RM, Triscott J, Arora GK, Kumar A, Tieu V, Pauli C, Reist M, Lew
791 RJ, *et al* (2021) PI5P4Ks drive metabolic homeostasis through peroxisome-mitochondria

792 interplay. *Dev Cell* 56: 1661-1676.e10

793 Ryan CS, Fine AL, Cohen AL, Schiltz BM, Renaud DL, Wirrell EC, Patterson MC, Boczek NJ, Liu
794 R, Babovic-Vuksanovic D, *et al* (2018) De Novo DNM1L Variant in a Teenager With
795 Progressive Paroxysmal Dystonia and Lethal Super-refractory Myoclonic Status Epilepticus.
796 *J Child Neurol* 33: 651–658

797 Schrader M, Costello JL, Godinho LF, Azadi AS & Islinger M (2016) Proliferation and fission of
798 peroxisomes - An update. *Biochim Biophys Acta* 1863: 971–983

799 Schrader M, Kamoshita M & Islinger M (2020) Organelle interplay-peroxisome interactions in
800 health and disease. *J Inherit Metab Dis* 43: 71–89

801 Sheffer R, Douiev L, Edvardson S, Shaag A, Tamimi K, Soiferman D, Meiner V & Saada A (2016)
802 Postnatal microcephaly and pain insensitivity due to a de novo heterozygous DNM1L
803 mutation causing impaired mitochondrial fission and function. *Am J Med Genet Part A* 170:
804 1603–1607

805 Smaili SS, Hsu YT, Sanders KM, Russell JT & Youle RJ (2001) Bax translocation to mitochondria
806 subsequent to a rapid loss of mitochondrial membrane potential. *Cell Death Differ* 8: 909–
807 920

808 Smirnova E, Griparic L, Shurland DL & van der Bliek AM (2001) Dynamin-related protein Drp1 is
809 required for mitochondrial division in mammalian cells. *Mol Biol Cell* 12: 2245–56

810 Spinelli JB, Rosen PC, Sprenger H-G, Puszynska AM, Mann JL, Roessler JM, Cangelosi AL,
811 Henne A, Condon KJ, Zhang T, *et al* (2021) Fumarate is a terminal electron acceptor in the
812 mammalian electron transport chain. *Science* 374: 1227–1237

813 Sugiura A, Mattie S, Prudent J & Mcbride HM (2017) Newly born peroxisomes are a hybrid of
814 mitochondrial and ER-derived pre-peroxisomes. *Nature* 542: 251–254

815 Taguchi N, Ishihara N, Jofuku A, Oka T & Mihara K (2007) Mitotic phosphorylation of dynamin-
816 related GTPase Drp1 participates in mitochondrial fission. *J Biol Chem* 282: 11521–11529

817 Tanaka H, Okazaki T, Aoyama S, Yokota M, Koike M, Okada Y, Fujiki Y & Gotoh Y (2019)
818 Peroxisomes control mitochondrial dynamics and the mitochondrion-dependent apoptosis
819 pathway. *J Cell Sci* 132

820 Valera-Alberni M, Joffraud M, Miro-Blanch J, Capellades J, Junza A, Dayon L, Núñez Galindo A,
821 Sanchez-Garcia JL, Valsesia A, Cercillieux A, *et al* (2021) Crosstalk between Drp1
822 phosphorylation sites during mitochondrial remodeling and their impact on metabolic
823 adaptation. *Cell Rep* 36

824 Vandeleur D, Chen C V., Huang EJ, Connolly AJ, Sanchez H & Moon-Grady AJ (2019) Novel and
825 lethal case of cardiac involvement in DNM1L mitochondrial encephalopathy. *Am J Med*
826 *Genet Part A* 179: 2486–2489

827 Vantaggiato C, Castelli M, Giovarelli M, Orso G, Bassi MT, Clementi E & De Palma C (2019) The
828 Fine Tuning of Drp1-Dependent Mitochondrial Remodeling and Autophagy Controls
829 Neuronal Differentiation. *Front Cell Neurosci* 13: 120

830 Vincent AE, White K, Davey T, Philips J, Ogden RT, Lawess C, Warren C, Hall MG, Ng YS,
831 Falkous G, *et al* (2019) Quantitative 3D Mapping of the Human Skeletal Muscle Mitochondrial
832 Network. *Cell Rep* 26: 996-1009.e4

833 Wai T & Langer T (2016) Mitochondrial Dynamics and Metabolic Regulation. *Trends Endocrinol*
834 *Metab* 27: 105–117 doi:10.1016/j.tem.2015.12.001 [PREPRINT]

835 Wakabayashi J, Zhang Z, Wakabayashi N, Tamura Y, Fukaya M, Kensler TW, Iijima M & Sesaki
836 H (2009) The dynamin-related GTPase Drp1 is required for embryonic and brain
837 development in mice. *J Cell Biol* 186: 805–816

838 Wang Y, Wang L, Zhu Y & Qin J (2018) Human brain organoid-on-a-chip to model prenatal
839 nicotine exposure. *Lab Chip* 18: 851–860

840 Wasiak S, Zunino R & McBride HM (2007) Bax/Bak promote sumoylation of DRP1 and its stable
841 association with mitochondria during apoptotic cell death. *J Cell Biol* 177: 439–450

842 Wasilewski M & Chacinska A (2021) MIC60 relays oxidation to block mitophagy. *Nat Metab 2021*
843 *39* 3: 1146–1147

844 Waterham HR, Ferdinandusse S & Wanders RJA (2016) Human disorders of peroxisome
845 metabolism and biogenesis. *Biochim Biophys Acta - Mol Cell Res* 1863: 922–933

846 Waterham HR, Koster J, van Roermund CWT, Mooyer PAW, Wanders RJA & Leonard J V. (2007)
847 A lethal defect of mitochondrial and peroxisomal fission. *N Engl J Med* 356: 1736–1741

848 Whitley BN, Lam C, Cui H, Haude K, Bai R, Escobar L, Hamilton A, Brady L, Tarnopolsky MA,
849 Dengle L, *et al* (2018) Aberrant Drp1-mediated mitochondrial division presents in humans
850 with variable outcomes. *Hum Mol Genet* 27: 3710–3719

851 Wilkens V, Kohl W & Busch K (2013) Restricted diffusion of OXPHOS complexes in dynamic
852 mitochondria delays their exchange between cristae and engenders a transitory mosaic
853 distribution. *J Cell Sci* 126: 103–116

854

Figure 1

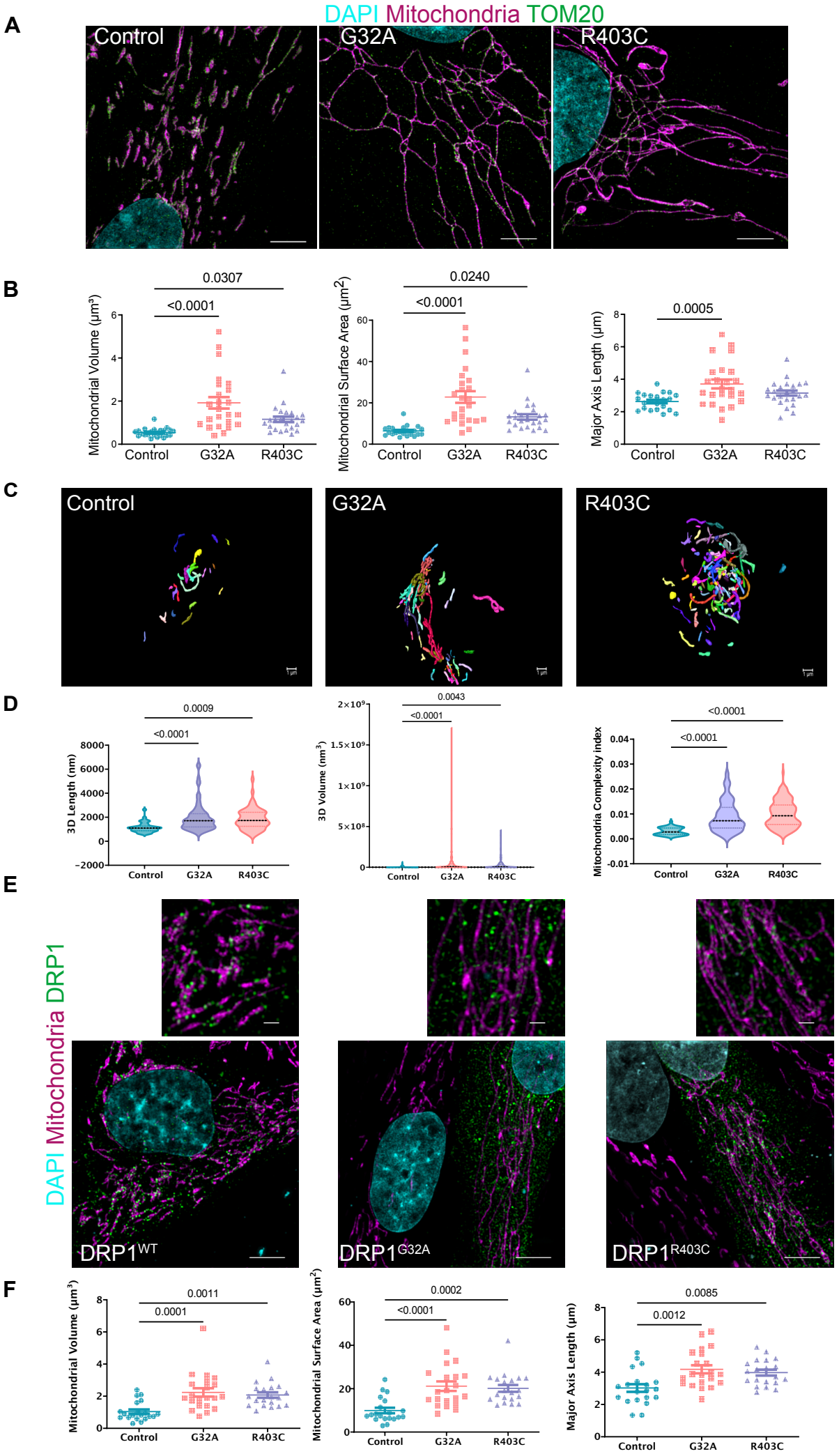
A
DAPI Mitochondria TOM20
Control
G32A
R403C
B
Mitochondrial Volume (µm³)
0.0307
<0.0001
Control
G32A
R403C
Mitochondrial Surface Area (µm²)
0.0240
<0.0001
Major Axis Length (µm)
0.0005
C
Control
G32A
R403C
D
3D Length (nm)
0.0009
<0.0001
3D Volume (nm³)
0.0043
<0.0001
Mitochondria Complexity index
<0.0001
<0.0001
E
DAPI Mitochondria DRP1
DRP1WT
DRP1G32A
DRP1R403C
F
Mitochondrial Volume (µm³)
0.0011
0.0001
Mitochondrial Surface Area (µm²)
0.0002
<0.0001
Major Axis Length (µm)
0.0085
0.0012

Figure 2

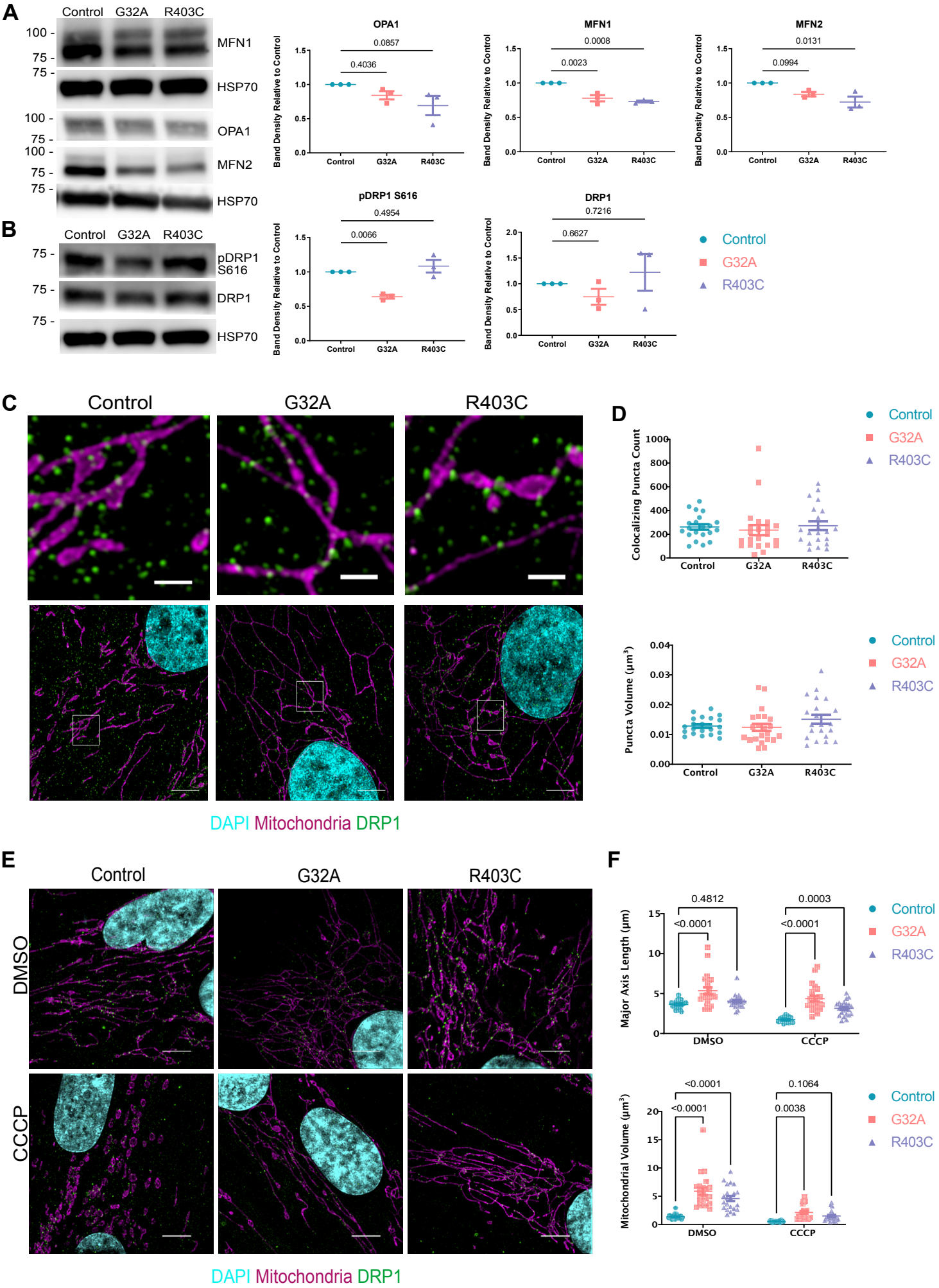
A
Control
G32A
R403C
100 -
75 -
MFN1
HSP70
OPA1
MFN2
Band Density Relative to Control
OPA1
0.0857
0.4036
MFN1
0.0008
0.0023
MFN2
0.0131
0.0994
B
pDRP1 S616
DRP1
pDRP1 S616
0.4954
0.0066
DRP1
0.7216
0.6627
Control
G32A
R403C
C
Control
G32A
R403C
DAPI Mitochondria DRP1
D
Colocalizing Puncta Count
Puncta Volume (μm³)
E
DMSO
CCCP
DAPI Mitochondria DRP1
F
Major Axis Length (μm)
0.4812
<0.0001
0.0003
<0.0001
Mitochondrial Volume (μm³)
<0.0001
<0.0001
0.1064
0.0038

Figure 3

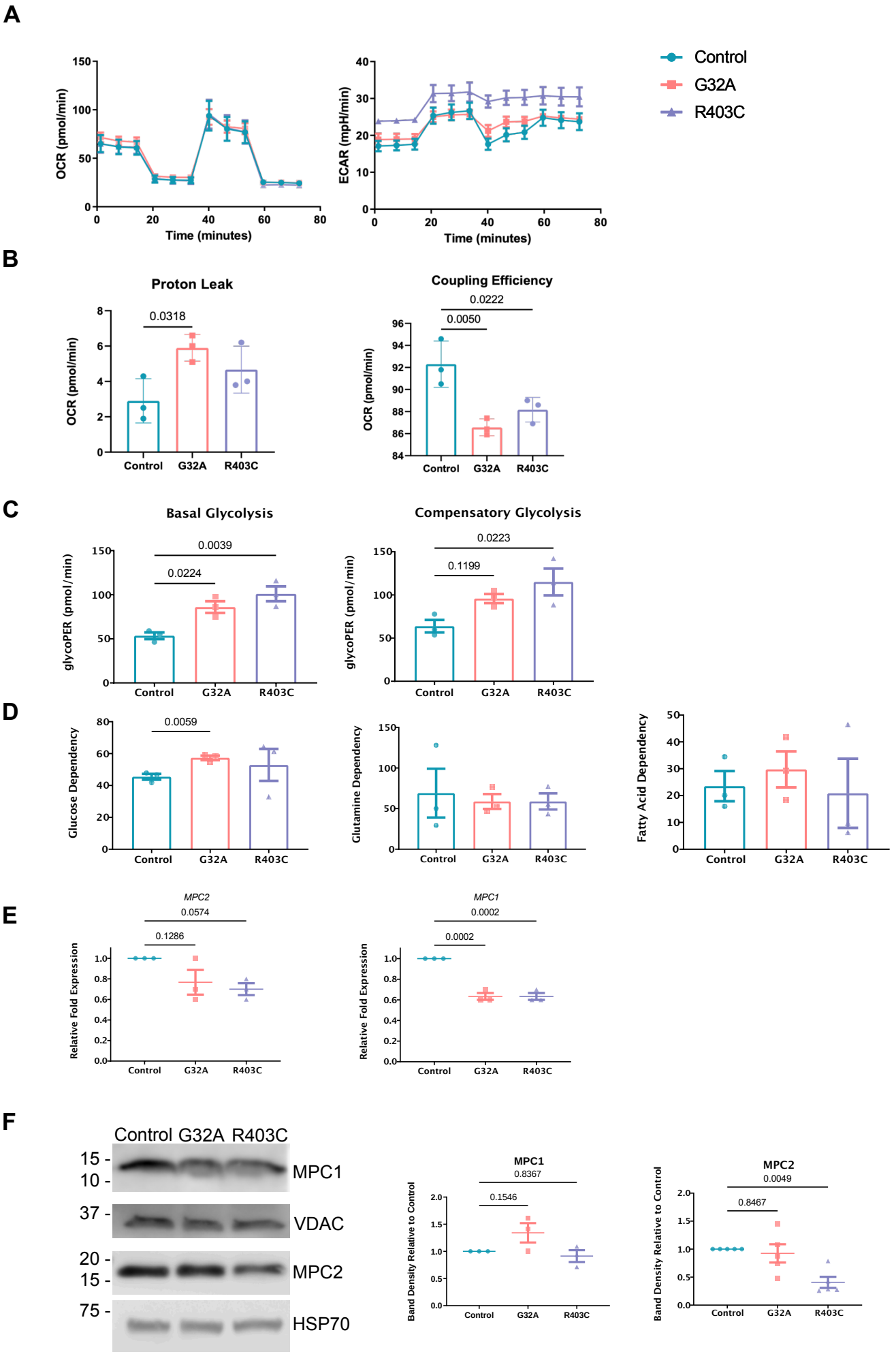
A
OCR (pmol/min)
Time (minutes)
ECAR (mpH/min)
Time (minutes)
Control
G32A
R403C
B
Proton Leak
OCR (pmol/min)
0.0318
Control
G32A
R403C
Coupling Efficiency
OCR (pmol/min)
0.0222
0.0050
Control
G32A
R403C
C
Basal Glycolysis
glycoPER (pmol/min)
0.0039
0.0224
Control
G32A
R403C
Compensatory Glycolysis
glycoPER (pmol/min)
0.0223
0.1199
Control
G32A
R403C
D
Glucose Dependency
0.0059
Control
G32A
R403C
Glutamine Dependency
Control
G32A
R403C
Fatty Acid Dependency
Control
G32A
R403C
E
MPC2
0.0574
0.1286
Relative Fold Expression
Control
G32A
R403C
MPC1
0.0002
0.0002
Relative Fold Expression
Control
G32A
R403C
F
Control G32A R403C
15 -
10 -
MPC1
37 -
VDAC
20 -
15 -
MPC2
75 -
HSP70
MPC1
0.8367
0.1546
Band Density Relative to Control
Control
G32A
R403C
MPC2
0.0049
0.8467
Band Density Relative to Control
Control
G32A
R403C

Figure 4

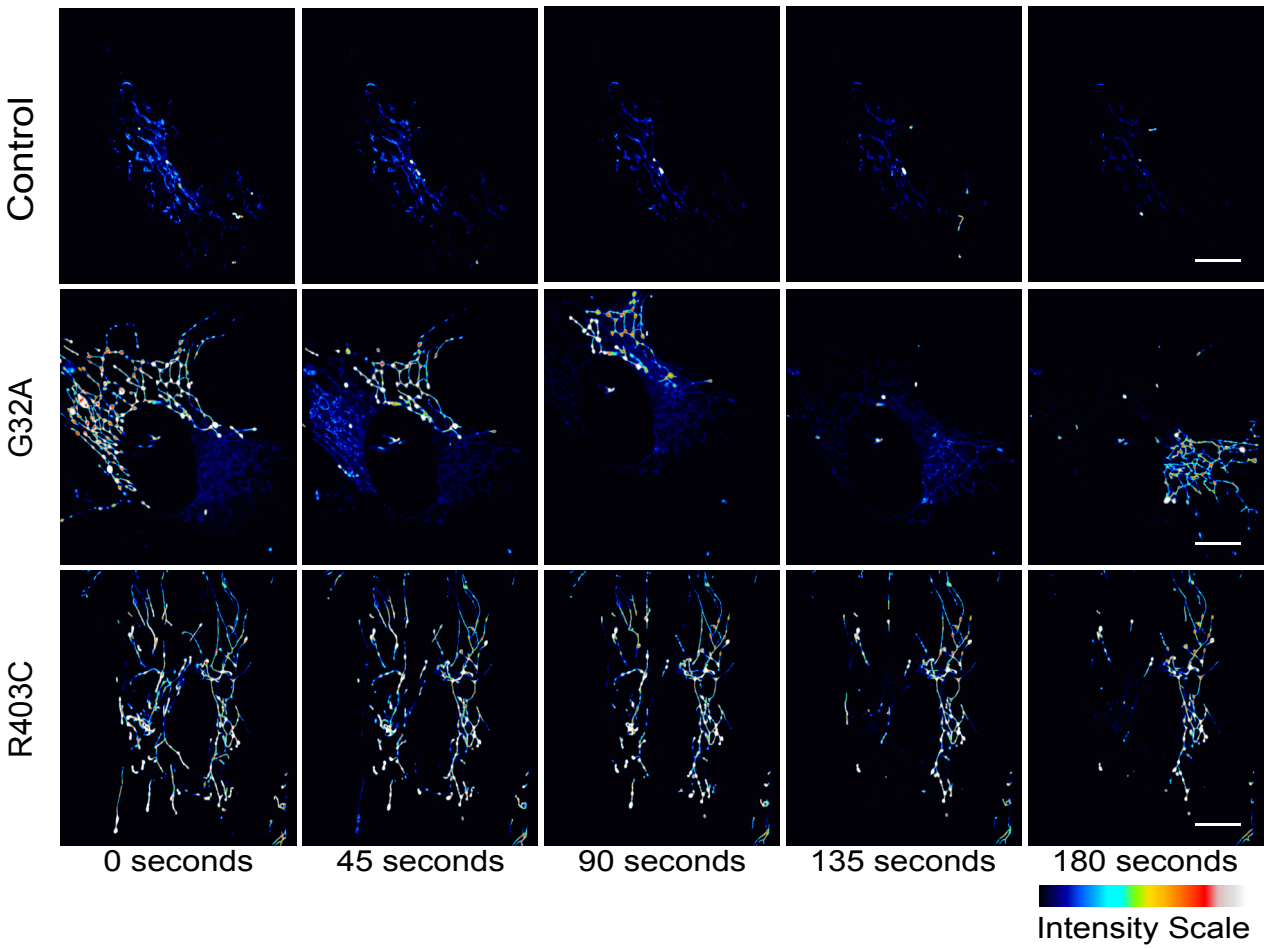
Control
G32A
R403C
0 seconds
45 seconds
90 seconds
135 seconds
180 seconds
Intensity Scale

Figure 5

A

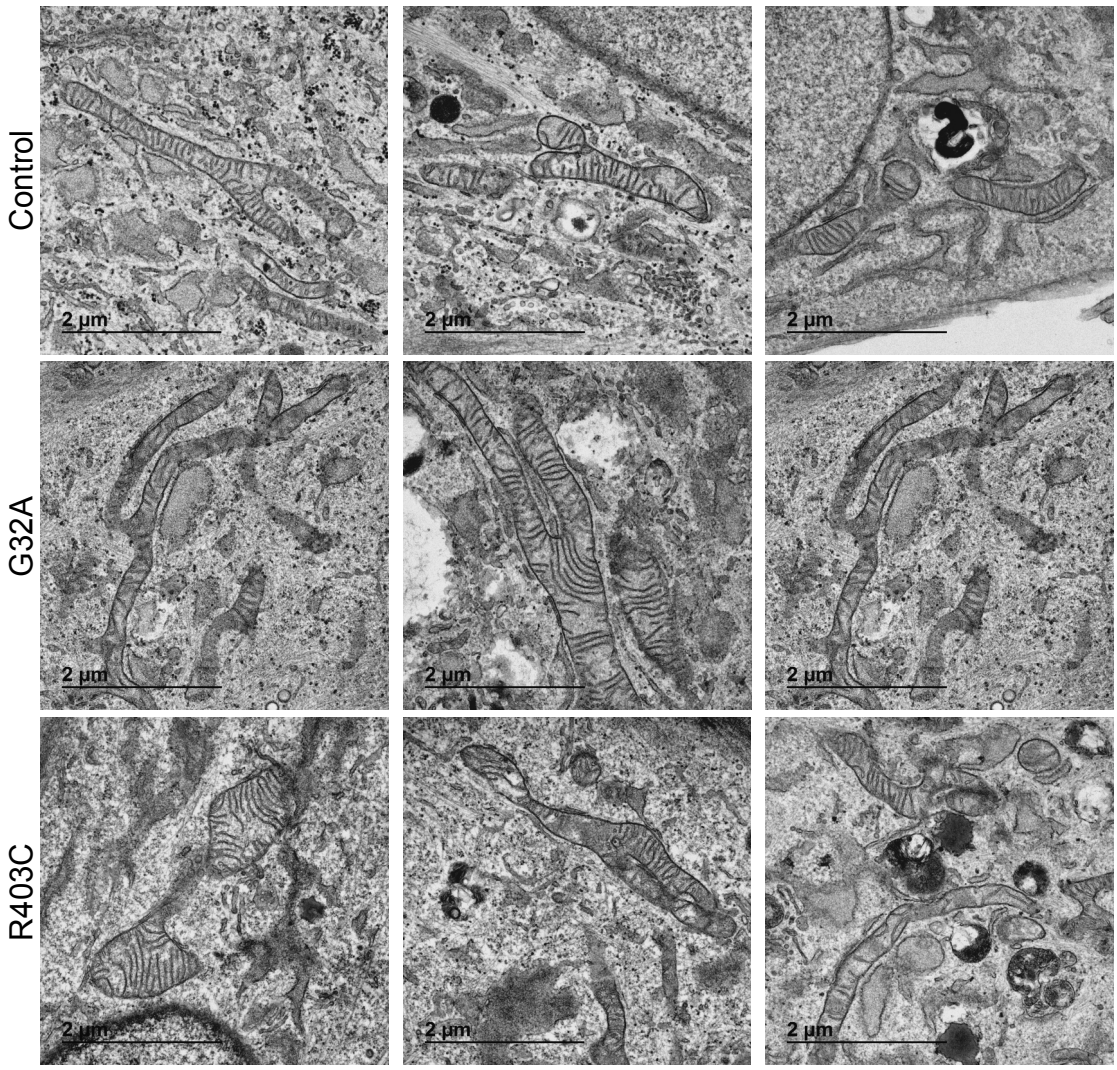
Control
G32A
R403C
2 µm

B

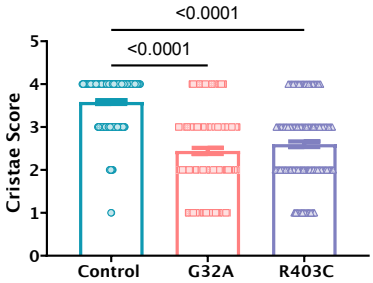
<0.0001
<0.0001
Cristae Score
0
1
2
3
4
5
Control
G32A
R403C

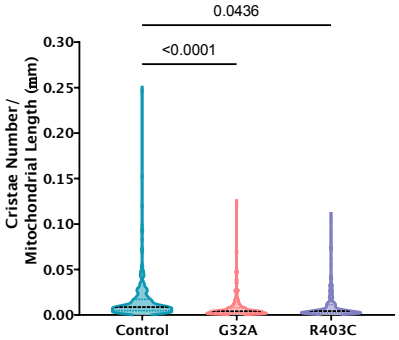
0.0436
<0.0001
Cristae Number/
Mitochondrial Length (µm)
0.00
0.05
0.10
0.15
0.20
0.25
0.30
Control
G32A
R403C

Figure 6

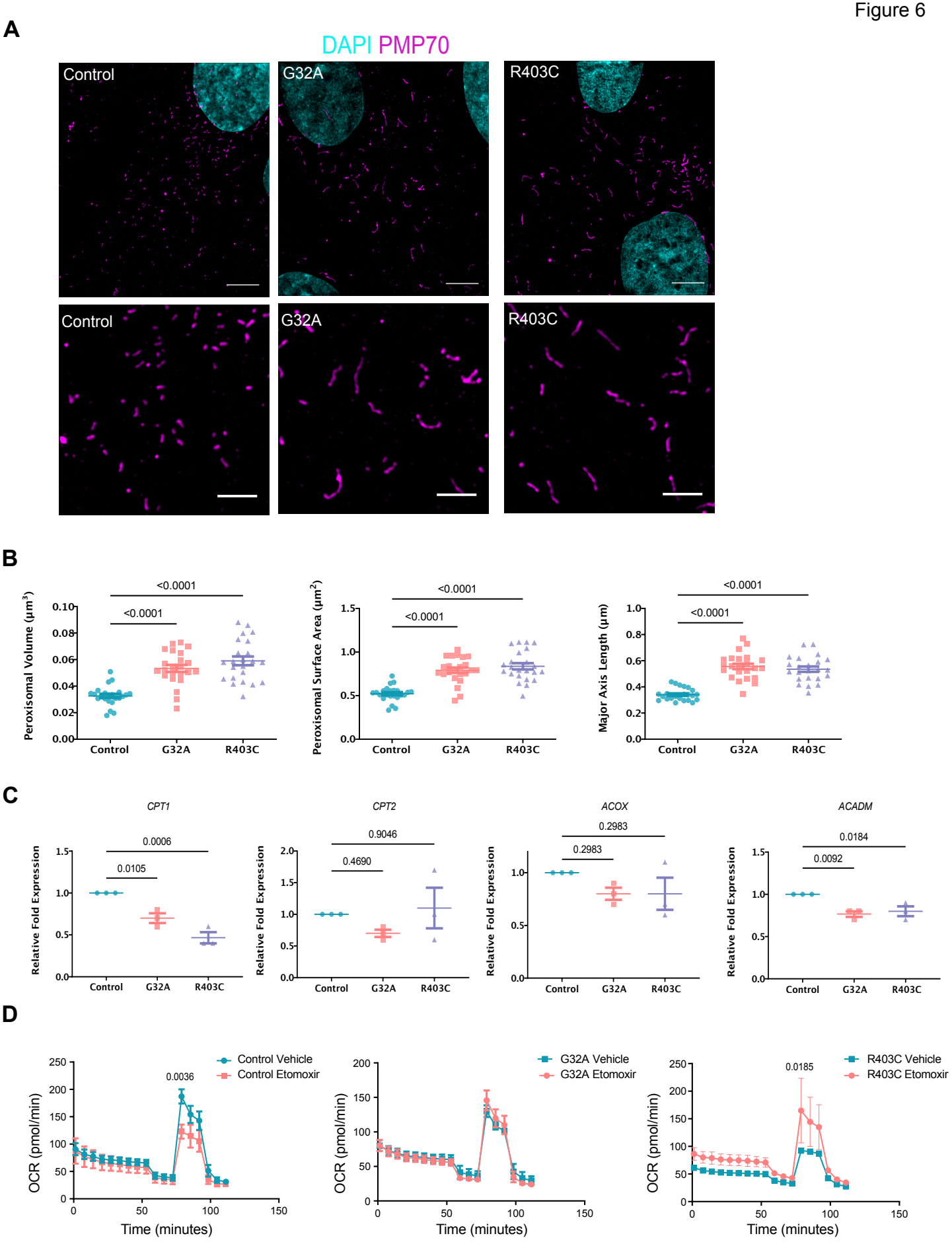
A
DAPI PMP70
Control
G32A
R403C
Control
G32A
R403C
B
Peroxisomal Volume (µm³)
<0.0001
<0.0001
Control
G32A
R403C
Peroxisomal Surface Area (µm²)
<0.0001
<0.0001
Control
G32A
R403C
Major Axis Length (µm)
<0.0001
<0.0001
Control
G32A
R403C
C
CPT1
Relative Fold Expression
0.0006
0.0105
Control
G32A
R403C
CPT2
Relative Fold Expression
0.9046
0.4690
Control
G32A
R403C
ACOX
Relative Fold Expression
0.2983
0.2983
Control
G32A
R403C
ACADM
Relative Fold Expression
0.0184
0.0092
Control
G32A
R403C
D
Control Vehicle
Control Etomoxir
0.0036
OCR (pmol/min)
Time (minutes)
G32A Vehicle
G32A Etomoxir
OCR (pmol/min)
Time (minutes)
R403C Vehicle
R403C Etomoxir
0.0185
OCR (pmol/min)
Time (minutes)

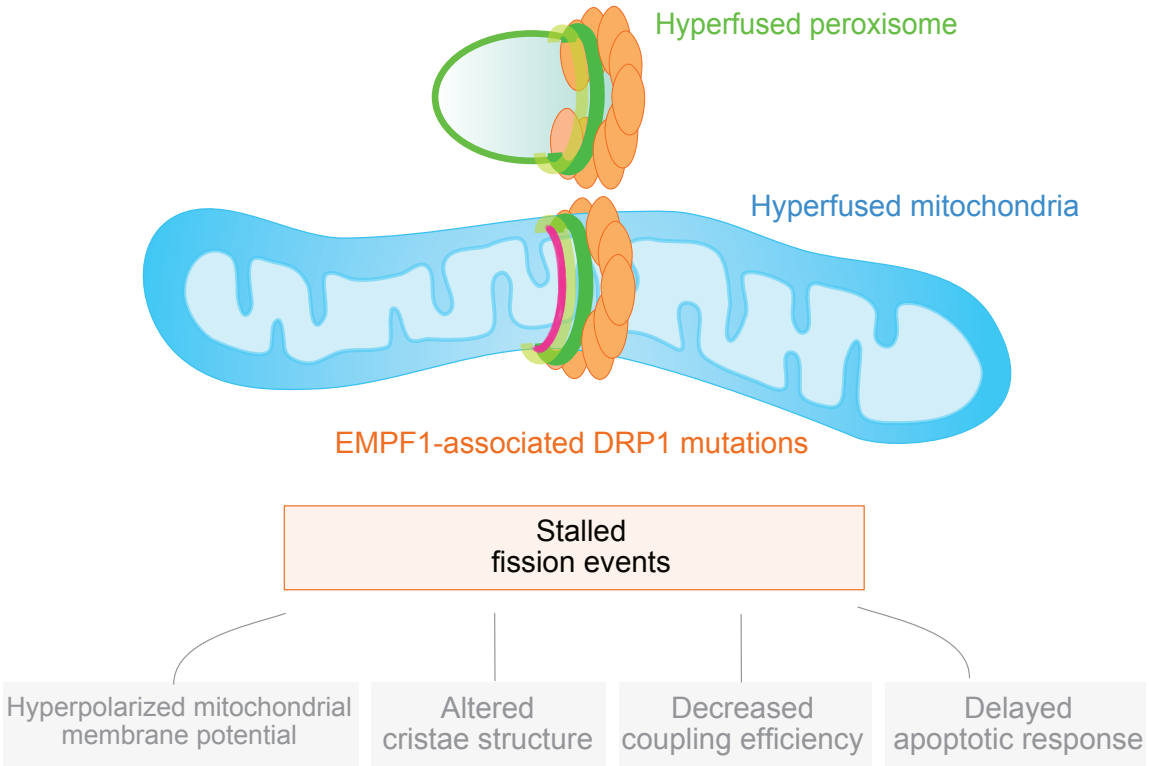
Hyperfused peroxisome
Hyperfused mitochondria
EMPF1-associated DRP1 mutations
Stalled
fission events
Hyperpolarized mitochondrial
membrane potential
Altered
cristae structure
Decreased
coupling efficiency
Delayed
apoptotic response